Astronomy & Astrophysics

The CARMENES search for exoplanets around M dwarfs

Different roads to radii and masses of the target stars[⋆]

A. Schweitzer[1], V. M. Passegger[1], C. Cifuentes[2,3], V. J. S. Béjar[4,5], M. Cortés-Contreras[2], J. A. Caballero[2],
C. del Burgo[6], S. Czesla[1], M. Kürster[7], D. Montes[3], M. R. Zapatero Osorio[8], I. Ribas[9,10], A. Reiners[11],
A. Quirrenbach[12], P. J. Amado[13], J. Aceituno[13,14], G. Anglada-Escudé[13,15], F. F. Bauer[13], S. Dreizler[11],
S. V. Jeffers[11], E. W. Guenther[16], T. Henning[7], A. Kaminski[12], M. Lafarga[9,10], E. Marfil[3], J. C. Morales[9,10],
J. H. M. M. Schmitt[1], W. Seifert[12], E. Solano[2], H. M. Tabernero[8,3], and M. Zechmeister[11]

[1] Hamburger Sternwarte, Gojenbergsweg 112, 21029 Hamburg, Germany
e-mail: aschweitzer@hs.uni-hamburg.de

[2] Departamento de Astrofísica, Centro de Astrobiología (CSIC-INTA), ESAC Campus, Camino Bajo del Castillo s/n, 28691 Villanueva de la Cañada, Madrid, Spain

[3] Departamento de Física de la Tierra y Astrofísica and UPARCOS-UCM (Unidad de Física de Partículas y del Cosmos de la UCM), Facultad de Ciencias Físicas, Universidad Complutense de Madrid, 28040 Madrid, Spain

[4] Instituto de Astrofísica de Canarias, Vía Láctea s/n, 38205 La Laguna, Tenerife, Spain

[5] Departamento de Astrofísica, Universidad de La Laguna, 38206 La Laguna, Tenerife, Spain

[6] Instituto Nacional de Astrofísica, Óptica y Electrónica, Luis Enrique Erro 1, Sta. Ma. Tonantzintla, Puebla, Mexico

[7] Max-Planck-Institut für Astronomie, Königstuhl 17, 69117 Heidelberg, Germany

[8] Centro de Astrobiología (CSIC-INTA), Carretera de Ajalvir km 4, 28850 Torrejón de Ardoz, Madrid, Spain

[9] Institut de Ciències de l'Espai (CSIC-IEEC), Can Magrans s/n, Campus UAB, 08193 Bellaterra, Barcelona, Spain

[10] Institut d'Estudis Espacials de Catalunya (IEEC), C/ Gran Capità 2-4, 08034 Barcelona, Spain

[11] Institut für Astrophysik, Georg-August-Universität, Friedrich-Hund-Platz 1, 37077 Göttingen, Germany

[12] Landessternwarte, Zentrum für Astronomie der Universität Heidelberg, Königstuhl 12, 69117 Heidelberg, Germany

[13] Instituto de Astrofísica de Andalucía (IAA-CSIC), Glorieta de la Astronomía s/n, 18008 Granada, Spain

[14] Centro Astronómico Hispano-Alemán (CSIC-MPG), Observatorio Astronómico de Calar Alto, Sierra de los Filabres, 04550 Gérgal, Almería, Spain

[15] School of Physics and Astronomy, Queen Mary, University of London, 327 Mile End Road, London E1 4NS, UK

[16] Thüringer Landessternwarte Tautenburg, Sternwarte 5, 07778 Tautenburg, Germany

ABSTRACT

Aims. We determine the radii and masses of 293 nearby, bright M dwarfs of the CARMENES survey. This is the first time that such a large and homogeneous high-resolution ($R > 80\,000$) spectroscopic survey has been used to derive these fundamental stellar parameters.

Methods. We derived the radii using Stefan–Boltzmann's law. We obtained the required effective temperatures T_{eff} from a spectral analysis and we obtained the required luminosities L from integrated broadband photometry together with the *Gaia* DR2 parallaxes. The mass was then determined using a mass-radius relation that we derived from eclipsing binaries known in the literature. We compared this method with three other methods: (1) We calculated the mass from the radius and the surface gravity $\log g$, which was obtained from the same spectral analysis as T_{eff}. (2) We used a widely used infrared mass-magnitude relation. (3) We used a Bayesian approach to infer stellar parameters from the comparison of the absolute magnitudes and colors of our targets with evolutionary models.

Results. Between spectral types M0 V and M7 V our radii cover the range $0.1\,R_{\odot} < R < 0.6\,R_{\odot}$ with an error of 2–3% and our masses cover $0.09\,\mathcal{M}_{\odot} < \mathcal{M} < 0.6\,\mathcal{M}_{\odot}$ with an error of 3–5%. We find good agreement between the masses determined with these different methods for most of our targets. Only the masses of very young objects show discrepancies. This can be well explained with the assumptions that we used for our methods.

Key words. stars: fundamental parameters – stars: low-mass – stars: late-type – stars: general

1. Introduction

The mass of a star is one of its most important properties. When trying to understand a star by itself and when isolating it from its environment, it is fundamental to stellar physics that the mass is the most influential parameter that determines almost exclusively all other properties throughout a star's life. Moreover, should the star have a companion, the masses of both components determine the gravitational potential and their orbits. In particular, if the companion is a planet, the gravitational potential is dominated by the stellar mass, which is crucial to know if we want to measure the minimum mass, $\mathcal{M}_P \sin i$, of the planet.

The latter is the situation that the CARMENES search faces in its quest to find Earth-mass planets. CARMENES (Calar Alto

---

high-Resolution search for M dwarfs with Exo-earths with Near-infrared and optical Échelle Spectrographs) is a double channel spectrograph built to find Earth-mass planets around M dwarfs using the radial-velocity method (Quirrenbach et al. 2014). The visual channel of this spectrograph has a resolving power of $R \approx 95\,000$ and covers the wavelength range from $0.52\,\mu m$ to $0.96\,\mu m$. Its near infrared channel has a resolving power of $R \approx 80\,000$ and covers the wavelength range from $0.96\,\mu m$ to $1.71\,\mu m$. This spectrograph is operated at the 3.5 m telescope on Calar Alto, Spain, and has been taking data since January 2016 (Quirrenbach et al. 2016, 2018; Reiners et al. 2018a). So far CARMENES has been used in the discovery of several new planets (Reiners et al. 2018b; Kaminski et al. 2018; Ribas et al. 2018; Luque et al. 2018; Nagel et al. 2019). All of these discoveries estimated the mass of the host star with the same procedure that we present in this work, even though Reiners et al. (2018b), Kaminski et al. (2018), and Ribas et al. (2018) used slightly older data than those used in this work. However, an in-depth investigation of the validity of this method is still missing.

A widely used method to determine masses of M dwarfs directly is the observation of detached double-lined eclipsing binary systems (see, e.g., Andersen 1991; Torres et al. 2010; Torres 2013, for reviews). Accurately measuring the radial-velocity amplitudes of the components of such systems allows us to derive their stellar masses independently. Another method to measure the masses of M dwarfs dynamically are observations of astrometric binaries that are also visual or spectroscopic binaries (see, e.g., Quirrenbach et al. 2001; Benedict et al. 2016, and both their references), for which it is possible to reconstruct the orbits of the components.

For measuring stellar radii, eclipsing binaries can be used as well. The radii of their components and the inclination of the system can be determined from the eclipsing light curve (e.g., Torres & Ribas 2002; Ribas 2003; Clausen et al. 2009; Morales et al. 2009). For single stars, interferometry is used to directly measure the angular diameter (e.g., van Belle et al. 2009; Boyajian et al. 2012a,b; Ligi et al. 2016). Together with the distance, the physical radius can be inferred from the same dataset. However, it is difficult to apply this method to low-mass stars because they are small and faint, which requires high sensitivity and resolution to achieve acceptable accuracy. Some interferometric radius measurements of M dwarfs with uncertainties of 1–5% have been performed by Ségransan et al. (2003), Berger et al. (2006), Boyajian et al. (2012b), and von Braun et al. (2014).

On the other hand, because the fundamental techniques of measuring the mass and radius of isolated M dwarfs (or those with wide companions) are limited, well-calibrated empirical relationships are generally employed. This is an adequate solution if the stars are assumed to behave like statistical representatives of the sample on which these relations are based. It has the advantage that only the luminosity or magnitude in certain bands has to be measured to estimate the stellar mass. An early mass-luminosity relation for M dwarfs was provided by Henry & Donald (1993). Several other works (e.g., Delfosse et al. 2000; Benedict et al. 2016; Mann et al. 2019) provided up-to-date mass-magnitude relations for low-mass stars, calibrated for different parameter ranges. Additionally, relations connecting colors or other measurable quantities with the mass or radius that are not directly accessible have been established to determine missing parameters of stars in question (e.g., Mann et al. 2015). If there are, however, systematic differences between the samples used to determine any such empirical

relation and the stars to be analyzed, then there is a bias in the results, which are based on such relations. Most prominently, the level of stellar activity may cause such a bias. For example, Caballero et al. (2010), Jackson et al. (2018), and Kesseli et al. (2018) reported inflated radii for young, magnetically active, or fast rotating stars.

Therefore, to obtain the mass $\mathcal{M}$ of the CARMENES targets we would traditionally use, for example, a $\mathcal{M}-M_K$ relation (e.g., Delfosse et al. 2000) and an infrared magnitude. This was actually done in the first CARMENES-based planet analysis (Trifonov et al. 2018) and in the survey overview of Reiners et al. (2018a). Our new approach, however, is to use such relations only when unavoidable. Instead, we exploit as much information from the observations as possible and use all the measurements, including our spectra and up-to-date photometry and parallaxes, already obtained. We also investigate the accuracy with which we can measure the radius and mass of a star. This includes calculating individual error bars for every analyzed object. We finally confront our method with other methods (both new and traditional) using the same homogeneous data set.

In Sect. 2 we present the sample used in this work. In Sect. 3 we describe our method. In short, we combine several purely observational data sets (high-resolution spectroscopy, photometry, and trigonometric parallaxes) with only one computational model (synthetic spectra based on a grid of model atmospheres) and one fundamental relation (a mass-radius relation) to obtain luminosities, radii, and masses. In Sect. 4 we compare the results from our method with results obtained from other alternative methods. In Sects. 5 and 6 we finally discuss the results and draw conclusions for the future.

2. The sample

To date, the catalog of targets observed during guaranteed time observations (GTO) of the CARMENES spectrograph includes a total of 341 bright, nearby M dwarfs or M dwarf systems, for which CARMENES based results have been published, and we use 293 of these for the reasons outlined below.

In this work we based our mass and radius determinations on the spectral analysis of Passegger et al. (2016; 2018, see Sect. 3.2). We imposed the same requirements and only used those CARMENES spectra with a signal-to-noise ratio (S/N) of $S/N > 75$. Furthermore, as in Passegger et al. (2018, hereafter Pass18) we excluded targets with spectral line profiles that cannot be reproduced by a purely photospheric model, i.e., stars with signs of activity that significantly affect the profiles of the lines used by Pass18 for determining stellar parameters; see Tal-Or et al. (2018) and Fuhrmeister et al. (2018) for the impact of activity on CARMENES target stars. Finally, as in Pass18 we excluded fast rotators. All these criteria finally yield 293 stars.

Previously, however, different CARMENES GTO samples have been studied. Reiners et al. (2018a) presented the initial sample of 324 CARMENES targets without any presumable companion closer than 5 arcsec, while Baroch et al. (2018) added nine double-lined spectroscopic binaries discovered in the survey. Baroch et al. (2018) determined their minimum masses and radii using methods suitable for spectroscopic binaries, but we do not consider these nine binaries in this work because we are interested only in isolated M dwarfs (or those with wide companions). One of the original 324 targets was recently determined to be a close astrometric binary as well (to be discussed in a future publication) and we do not consider it in this work either. There can still be some very long-period, low-amplitude, single-lined spectroscopic binaries in our GTO
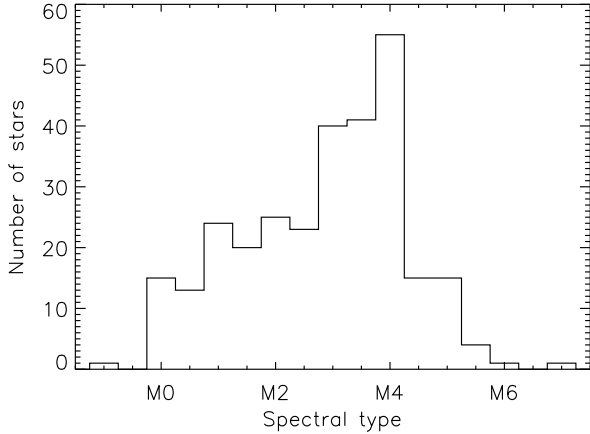
Fig. 1. Histogram of the spectral types (as determined by Alonso-Floriano et al. 2015, and references therein) of all 293 targets of our sample. The leftmost bin represents the only K7 V star in our sample.

sample that are yet to be discovered and did not pass our initial filters (Cortés-Contreras et al. 2017; Jeffers et al. 2018; Baroch et al. 2018). Another eight objects did not have any or not sufficient observations to reach enough S/N to be tabulated by Reiners et al. (2018a). Three of these[1] were included in the sample of Díez Alonso et al. (2019), who studied the rotation periods of CARMENES targets. All of these eight objects except one[2] were included in the study of Schöfer et al. (2019), who investigated the activity of the CARMENES targets. We, finally, included six[3] of the eight new targets.

We present our sample in Table B.1. For each of the 293 M dwarfs, we provide for identification purposes the CARMENES identifier (Caballero et al. 2016), the Gliese or Gliese & Jahreiss name when available, or the discovery name otherwise; we also give the luminosity-class V spectral type (Alonso-Floriano et al. 2015, and references therein). A histogram of the spectral types of our sample is shown in Fig. 1.

3. Our method

Our method is a multi-step process. In the first step in Sect. 3.1 we determine the luminosity from distance and photometry. In the second step in Sect. 3.2 we measure the effective temperature from the CARMENES spectra by fitting PHOENIX (Hauschildt & Baron 1999) synthetic spectra. In the third step in Sect. 3.3 we use Stefan–Boltzmann's law to obtain the radius. To finally obtain the masses in Sect. 3.4, we introduce an empirical mass-radius relation to calculate the mass from the radius. These steps, along with those needed for the alternative methods, are sketched in Fig. 2.

3.1. Distances and luminosities

We determine the luminosities from apparent magnitudes and distances. For 285 of the 293 M dwarfs, we retrieve parallactic

distances from the *Gaia* DR2 catalog (Gaia Collaboration 2018). For the remaining eight cases, which are not part of *Gaia* DR2 and are listed in Table B.1 together with a corresponding note, we retrieve parallactic distances from the astrometric analyses of van Altena et al. (1995, two stars[4]), van Leeuwen (2007, three stars[5]), and Finch & Zacharias (2016, two stars[6]), and derive spectrophotometric distances after applying the *J*-band absolute magnitude-spectral type relation given by Cortés-Contreras et al. (2017, one star[7]).

For every target star in the CARMENES input catalog Carmencita (Caballero et al. 2016), we collected apparent magnitudes in broadband passbands from a number of all-sky and ultra-wide surveys from the ultraviolet, through optical and near-infrared, to the mid-infrared. The integration of the spectral energy distribution (SED) of each CARMENES target allowed us to determine the bolometric luminosity L. In our case, we performed the integration with the Virtual Observatory SED Analyzer (VOSA; Bayo et al. 2008), the distances described above, and the SEDs built with photometric data from GALEX (FUV NUV; Morrissey et al. 2007), SDSS (*ugriz*; York et al. 2000), UCAC4 and APASS9 (*BgVri*; Zacharias et al. 2013; Henden et al. 2015), *Tycho*-2 (B_T V_T; Høg et al. 2000), *Gaia* DR2 (B_P G R_P; Gaia Collaboration 2018), CMC15 (*r′*; Muiños & Evans 2014), Pan-STARRS1 (*grizy*; Tonry et al. 2012), 2MASS (*JHK_s*; Skrutskie et al. 2006), and AllWISE (*W*1 *W*2 *W*3 *W*4; Cutri 2014). The VOSA software uses the latest zero-point fluxes provided by the Filter Profile Service (Rodrigo et al. 2012), which can be found on their website[8]. We used synthetic photometry based on the BT-Settl models (Allard et al. 2012) for the ultraviolet flux blueward of the Johnson *B* band and for the mid- and far-infrared redward of WISE *W*4. At the considered effective temperatures, M dwarfs hardly emit any flux in these two wavelength regions. Therefore, the approximation of these two contributions to the luminosity are barely dependent on the models chosen as input to VOSA. Moreover, by using synthetic photometry for the ultraviolet we do not contaminate the photospheric flux with chromospheric flux from stellar activity. The resulting luminosities are listed in Table B.1. Typical relative errors of L are between 1 and 2%. More details on the photometry compilation and luminosity derivation including their errors will be provided in a separate publication.

3.2. Effective temperatures, surface gravities, and metallicities

We measured the photospheric parameters effective temperature T_{eff}, surface gravity $\log g$, and metallicity, denoted by the relative iron abundance [Fe/H] by fitting PHOENIX-ACES synthetic spectra (Husser et al. 2013) to the CARMENES spectra of the visual (VIS) channel as described in Passegger et al. (2016) and Pass18. In summary, this method has T_{eff} and [Fe/H] as free parameters, but fixes $\log g$ by a $T_{eff} - \log g$ relation from theoretical 5 Gyr isochrones of Baraffe et al. (1998). To analyze all 293 members of our sample described in Sect. 2, we repeated the analysis of Pass18 using the latest available CARMENES

---

[1] J15474−108 (GJ 3916), J18198−019 (Gl 710) and J20556−140S (Gl 810B).

[2] J18198−019 (Gl 710).

[3] J04219+213 (K2-155), J08409−234 (Gl 317), J09143+526 (Gl 338A), J15474−108 (GJ 3916), J18198−019 (Gl 710) and J20556−140S (Gl 810B).

[4] J22020−194 (Gl 843) and J18224+620 (GJ 1227).

[5] J07274+052 (Gl 273), J11033+359 (Gl 411) and J11054+435 (Gl 412A).

[6] J06574+740 (2M J06572616+7405265) and J09133+688 (G 234-057).

[7] J06396−210 (LP 780-032).

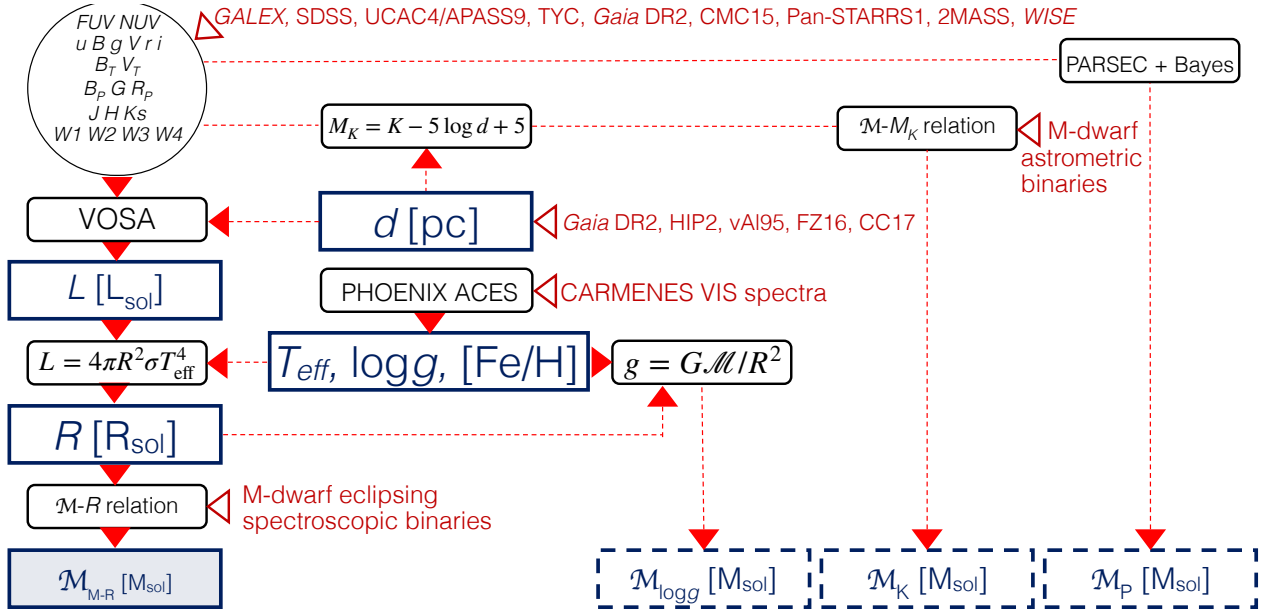[8] http://svo2.cab.inta-csic.es/theory/fps/

Fig. 2. Flowchart of our different roads to masses.

co-added (Zechmeister et al. 2018) VIS spectra that fulfill the requirements of Pass18 described above (cf. Sect. 2).

Pass18 presented the stellar photospheric parameters for 235 stars of our exoplanet survey. These authors used CARMENES VIS data for 234 targets and CAFE (Calar Alto Fiber-fed Echelle spectrograph) data for one star. We present in this work 59 new parameter sets derived from CARMENES spectroscopy, and update the parameters for 234 stars of Pass18 (omitting the binary mentioned in Sect. 2). The updated and Pass18 results agree within their fixed error bars ($\Delta T_{\rm eff}$ = 51 K, $\Delta \log g$ = 0.07 dex, and Δ[Fe/H] = 0.16 dex). All results are listed in Table B.1.

There exist, however, alternative model atmospheres and synthetic spectra for M dwarfs, most prominently the BT-Settl models (Allard et al. 2012). When they are used in spectral analyses, the fit quality (see, e.g., Rojas-Ayala et al. 2012) is similar to the fit quality in Pass18. However, the resulting photospheric parameters typically differ. Most recently, Rajpurohit et al. (2018) determined effective temperatures for the CARMENES GTO targets listed in Reiners et al. (2018a) using the latest BT-Settl models, which are about 100–200 K smaller than ours. Describing these differences is beyond the scope of this paper and they will be investigated in a future publication. However, in order to assess an error estimate resulting from the use of one specific set of synthetic spectra we repeated our analysis described above using the latest, publicly available grid with varying metallicities, which are the 2011 BT-Settl models. We then found effective temperatures that are about 50 K (i.e., our $\Delta T_{\rm eff}$) hotter for $T_{\rm eff} \lesssim 3700$ K and up to about 200 K cooler for $T_{\rm eff} \gtrsim 3700$ K. Owing to error propagation, this means that for $T_{\rm eff} \lesssim 3700$ K the derived radii and masses (see below) that are based on PHOENIX-ACES models, and radii and masses that are based on BT-Settl models would agree within our error bars. However, for higher $T_{\rm eff}$ values, there would be a systematic offset between these derived quantities. Similarly, using the significantly and systematically differing $T_{\rm eff}$ results from Rajpurohit et al. (2018) would also introduce a systematic offset in radii and masses beyond our error bars.

3.3. Radii

Using the effective temperature $T_{\rm eff}$ and luminosity L from Sect. 3.1 we calculated the radius R using Stefan–Boltzmann's law

$$R = \left(\frac{L}{4\pi\sigma T_{\rm eff}^4} \right)^{1/2} . \tag{1}$$

The error for R is then described by

$$\left(\frac{\Delta R}{R} \right)^2 = \left(2\, \frac{\Delta T_{\rm eff}}{T_{\rm eff}} \right)^2 + \left(\frac{1}{2} \frac{\Delta L}{L} \right)^2 . \tag{2}$$

When explicitly expressing L by the distance d and the photometrically measured flux S via $L = 4\pi d^2 \cdot S$ the radius becomes

$$R = \left(\frac{S}{\sigma T_{\rm eff}^4} \right)^{1/2} d \tag{3}$$

and thus

$$\left(\frac{\Delta R}{R} \right)^2 = \left(2\, \frac{\Delta T_{\rm eff}}{T_{\rm eff}} \right)^2 + \left(\frac{1}{2} \frac{\Delta S}{S} \right)^2 + \left(\frac{\Delta d}{d} \right)^2 . \tag{4}$$

In the era of satellite-based parallaxes, the relative error in distance $\Delta d/d$ is negligible except for the very few stars without *Gaia* DR2 or Hipparcos parallaxes. Therefore, the main contributions to the relative error arise from the precision of the measured effective temperature, $\Delta T_{\rm eff}/T_{\rm eff}$, and photometry $\Delta S/S$, which are both typically between 1 and 2 %, yielding typical $\Delta R/R$ between 2 and 3 %.

Our sample has 11 stars in common with the sample of stars with interferometric radii presented by Boyajian et al. (2012b). We used the interferometric angular diameter corrected for limb darkening $\Theta_{\rm LD}$ given in Boyajian et al. (2012b), but use *Gaia* DR2 distances d when available to calculate an interferometric radius $R_{\rm interf}$ via

$$R_{\rm interf} = \frac{1}{2} \Theta_{\rm LD} d. \tag{5}$$

Table 1. Radii of 11 stars of our sample with interferometric diameters measured by Boyajian et al. (2012b).

Karmn	Name	R $(R_\odot)$	R_{interf} $(R_\odot)$	Θ_{LD} [B] (mas)	d (pc)
J00183+440	Gl 15A	0.393 ± 0.011	0.385 ± 0.002	1.005 ± 0.005	3.5626 ± 0.0005 [G]
J05314-036	Gl 205	0.549 ± 0.029	0.578 ± 0.002	0.943 ± 0.004	5.7003 ± 0.0023 [G]
J09143+526	Gl 338A	0.578 ± 0.020	0.568 ± 0.010	0.834 ± 0.014	6.3339 ± 0.0016 [G]
J09144+526	Gl 338B	0.584 ± 0.019	0.583 ± 0.011	0.856 ± 0.016	6.3335 ± 0.0016 [G]
J11033+359	Gl 411	0.359 ± 0.016	0.392 ± 0.004	1.432 ± 0.013	2.5469 ± 0.0043 [HIP]
J11054+435	Gl 412A	0.375 ± 0.011	0.398 ± 0.009	0.764 ± 0.017	4.8480 ± 0.0235 [HIP]
J11421+267	Gl 436	0.427 ± 0.013	0.437 ± 0.014	0.417 ± 0.013	9.7561 ± 0.0086 [G]
J13457+148	Gl 526	0.470 ± 0.015	0.488 ± 0.008	0.835 ± 0.014	5.4354 ± 0.0015 [G]
J15194-077	Gl 581	0.308 ± 0.010	0.302 ± 0.009	0.446 ± 0.014	6.2992 ± 0.0020 [G]
J17578+046	Gl 699	0.185 ± 0.006	0.187 ± 0.001	0.952 ± 0.005	1.8267 ± 0.0010 [G]
J22565+165	Gl 880	0.527 ± 0.015	0.549 ± 0.003	0.744 ± 0.004	6.8677 ± 0.0019 [G]

References. [B] Boyajian et al. (2012b); [G] Gaia Collaboration (2018); [HIP] van Leeuwen (2007).
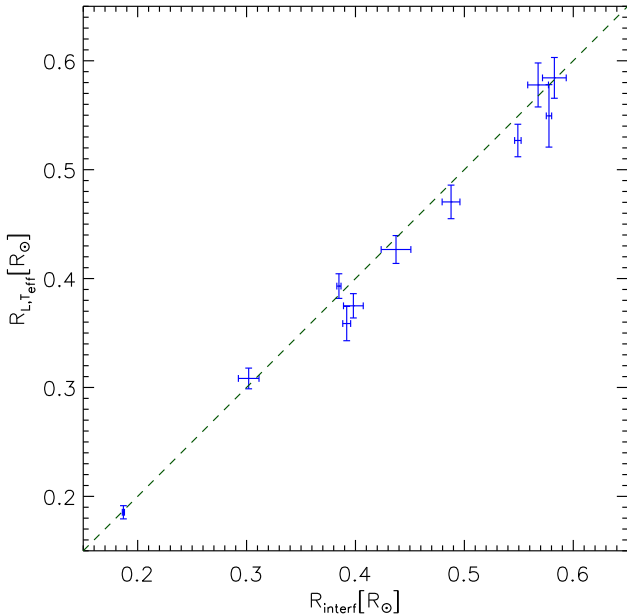

Fig. 3. Radii determined using the spectroscopic T_{eff} from Sect. 3.2, the bolometric luminosity from Sect. 3.1, and Stefan–Boltzmann's law plotted against interferometric radii from Boyajian et al. (2012b). The two discussed outliers are Gl 411 and Gl 412A with R_{interf} of 0.392 and 0.398 $R_\odot$, respectively.

These R_{interf} are listed in Table 1 along with the angular diameters and distances that we used. When we compared our spectroscopic radii with R_{interf} we find good agreement for 9 of the common stars, as can be seen in Fig. 3. Six of our radii have error bars comparable to the error bars obtained from interferometry. For the remaining 5 stars, interferometry is more precise, as expected. Only the radii of the 2 targets Gl 411 (J11033+359) and Gl 412A (J11054+435), which are based on Hipparcos parallaxes, differ significantly beyond their respective error bars (see Sect. 5.2). The parallactic distances for the other 9 M dwarfs are based on *Gaia* DR2 data.

3.4. Masses ($\mathcal{M}_{\mathcal{M}-R}$)

We compiled a sample of 55 detached, double-lined, double-eclipsing, main-sequence M dwarf binaries from the literature

(see Table B.2 and Fig. 4). We excluded pre-main-sequence stars in very young open clusters and very old stars in globular clusters. From the published masses and radii of these eclipsing binaries, we estimated the best linear fit (following Press et al. 2007) of the mass-radius relation and found for the radius and mass range given by Table B.2,

$$\frac{\mathcal{M}}{\mathcal{M}_\odot} = (-0.0240 \pm 0.0076) + (1.055 \pm 0.017) \cdot \frac{R}{R_\odot}, \quad (6)$$

or equivalently

$$\frac{R}{R_\odot} = (0.0282 \pm 0.0068) + (0.935 \pm 0.015) \cdot \frac{\mathcal{M}}{\mathcal{M}_\odot}. \quad (7)$$

Both fits have a non-reduced $\chi^2 \approx 0.02$ translating into an rms ≈ 0.02 in solar units.

By excluding members of young clusters, the mass-radius relation is well defined for M dwarfs older than a few hundred million years. This is underlined by the comparison with mass-radius relations for ages between 0.2 and 13 Gyr from evolutionary models for solar metallicity by Baraffe et al. (2015, hereafter BHAC15), also shown in Fig. 4. The explanation of the small difference between models and observations is beyond the scope of this paper. However, the small spread between the isochrones demonstrates that our linear mass-radius relation can be treated independently of age. Furthermore, our sample in Table B.2 includes all known eclipsing binaries in the field, independent of metallicity. Yet, our mass-radius relation is well defined, and, therefore, we conclude that it does not significantly depend on metallicity either. Such metallicity independence of the mass-radius relation for low-mass stars is also frequently found in evolutionary models (see, e.g., Fig. 3 of del Burgo & Allende Prieto 2018). This is underlined by including three representative low-metallicity members of the open clusters M 4, M 55, and NGC 6362 in Fig. 4 (but not in the fits for Eqs. 6 and 7), which match our mass-radius relation very well.

The reasons for the intrinsic spread in the observed mass-radius relation and the comparison to theoretical models have been and are still being investigated elsewhere (e.g., Feiden & Chaboyer 2012; Korda et al. 2017; Tognelli et al. 2018; Parsons et al. 2018). As pointed out by Parsons et al. (2018), this spread sets a lower limit on the error bars for the masses obtained with this method. In any case, for this paper, we
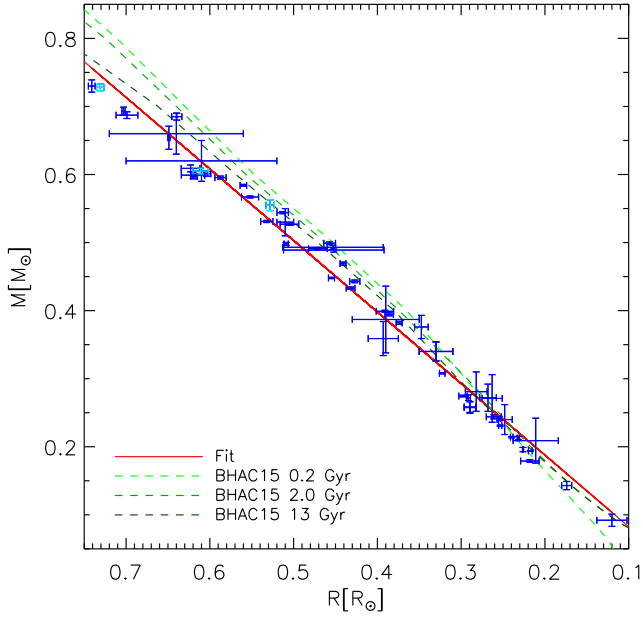
Fig. 4. Masses and radii for the eclipsing binaries of Table B.2. Blue crosses indicate field stars, while turquoise crosses indicate, *from left to right*, the low-metallicity globular cluster members NGC 6362 V41 B (Kaluzny et al. 2015), M4 V65 B (Kaluzny et al. 2013), and M55 V54 B (Kaluzny et al. 2014). The red solid line shows our best linear fit. The increasingly darker green dashed lines represent isochrones for 0.2, 2, and 13 Gyr from BHAC15.

assume that eclipsing binaries are representative of our single-star sample, and we apply our mass-radius relation to derive masses.

In Table B.1 and for the remainder of this paper we label masses determined with this method as $\mathcal{M}_{M-R}$. As already mentioned in the introduction, these are the masses that we have been using for the planet discoveries of CARMENES. However, Kaminski et al. (2018) used the effective temperature from Pass18. Reiners et al. (2018b) and Ribas et al. (2018) additionally used the mass-radius relation from Casal (2014) and the distances listed in *Gaia* DR1 (Gaia Collaboration 2016) or as measured by Hipparcos (van Leeuwen 2007) for calculating the luminosity. As a consequence, the masses we list for these three planet hosts[9] are about 5–8% higher than in the discovery papers. The largest contribution to this change is the update of the parallax and, hence, luminosity.

4. Comparison methods

4.1. Spectroscopic masses ($\mathcal{M}_{\log g}$)

If we use the surface gravity $\log g$ from Sect. 3.2, the mass is calculated via

$$\mathcal{M} = \frac{10^{\log g} R^2}{G},\tag{8}$$

and its error is calculated via

$$\left(\frac{\Delta \mathcal{M}}{\mathcal{M}}\right)^2 = (\ln 10 \, \Delta \log g)^2 + \left(2\,\frac{\Delta R}{R}\right)^2.\tag{9}$$

In practice, the error in $\log g$ dominates the error in $\mathcal{M}$. The precision of our radii $\Delta R/R$ is about 2–3% (cf. Sect. 3.3). It would

_____

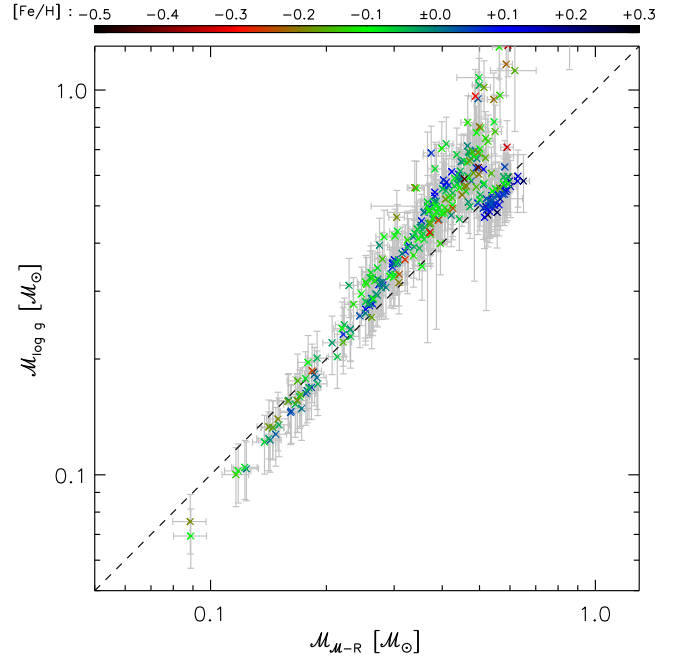[9] J16167+672S (Gl 617A), J17578+046 (Gl 699), J1919+051N (Gl 752A).

Fig. 5. Comparison of masses for all stars in Table B.1 using our two methods described in Sect. 4.1 on the *y*-axis and Sect. 3.4 on the *x*-axis. See Fig. A.1 for the same plot without error bars and linear axes.

require $\Delta \log g \lesssim 0.03$ dex for both contributions to Eq. (9) to become of similar size. However, our current $\Delta \log g = 0.07$ dex is about twice as large. In Table B.1 and for the remainder of this paper we label the mass determined with this method as $\mathcal{M}_{\log g}$.

We compare $\mathcal{M}_{M-R}$ from above with $\mathcal{M}_{\log g}$ in Fig. 5. We find systematically lower $\mathcal{M}_{\log g}$ values for the lowest ($\mathcal{M}_{M-R} \lesssim 0.2\,\mathcal{M}_\odot$) and highest ($\mathcal{M}_{M-R} \gtrsim 0.5\,\mathcal{M}_\odot$) $\mathcal{M}_{M-R}$ values. In between, the $\mathcal{M}_{\log g}$ values are higher than the $\mathcal{M}_{M-R}$ values, and in particular for $\mathcal{M}_{M-R}$ between 0.4 and 0.5 $\mathcal{M}_\odot$ there is a large scatter without any correlation, except for the highest metallicities, which seem to form a curve with a sharp turn around 0.5 $\mathcal{M}_\odot$.

Furthermore, we reverse the calculation and obtain the surface gravity from $\mathcal{M}_{M-R}$ and Stefan–Boltzmann's radius of Sect. (3.3). We call this $\log g_c$ and list this value in Table B.1 as well. When we compare the spectroscopic $\log g$ from Sect. 3.2 to this $\log g_c$ in Fig. 6 we find, as expected, a similar behavior as above when comparing $\mathcal{M}_{M-R}$ with $\mathcal{M}_{\log g}$: there is a large scatter in the mid-value regime but there are consistent results for the highest and lowest surface gravities, i.e., the least and most massive stars. And, again, the highest metallicity stars form a curve with less scatter than the other metallicities. This is a similar result as found by Pass18 in their Fig. 6, where some spectroscopic $\log g$ values deviate from literature values in a similar fashion. Also similar to Pass18 and as mentioned in Sect. 3.2, our $\log g$ is connected to $T_{\rm eff}$. This metallicity dependent connection causes systematic effects due to the underlying evolutionary models. In particular, the $\log g$ values for high-metallicity results are obtained by extrapolating from solar metallicity isochrones (Pass18).

To examine whether $\log g_c$ is more reliable than $\log g$, we compare our $\log g_c$ with literature values in Fig. 7 to produce a similar plot as Fig. 6 of Pass18. When comparing Fig. 6 of Pass18 to our Fig. 7 we find an improvement. The values published by Maldonado et al. (2015) generally agree well with our $\log g_c$. The $\log g$ values derived from radii and masses published
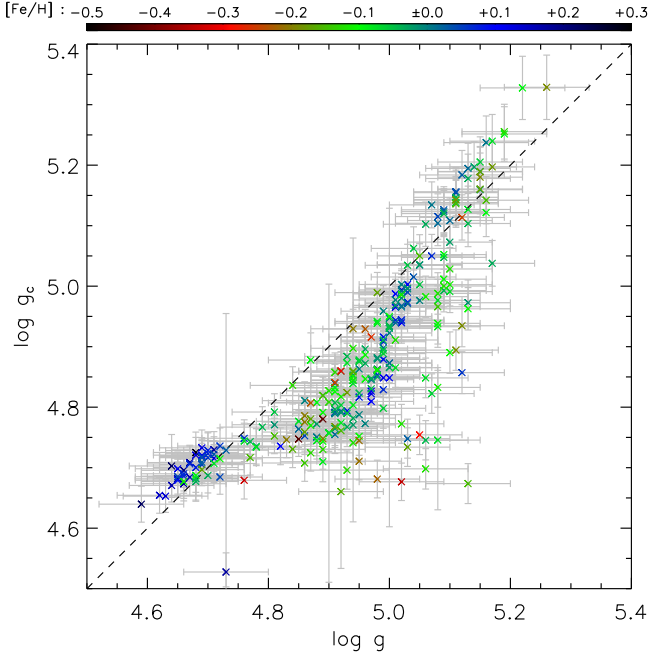
Fig. 6. Value of $\log g_c$ calculated using $\mathcal{M}_{M-R}$ from Sect. 3.4 and using R from Sect. 3.3 against the spectroscopic $\log g$ from Sect. 3.2.
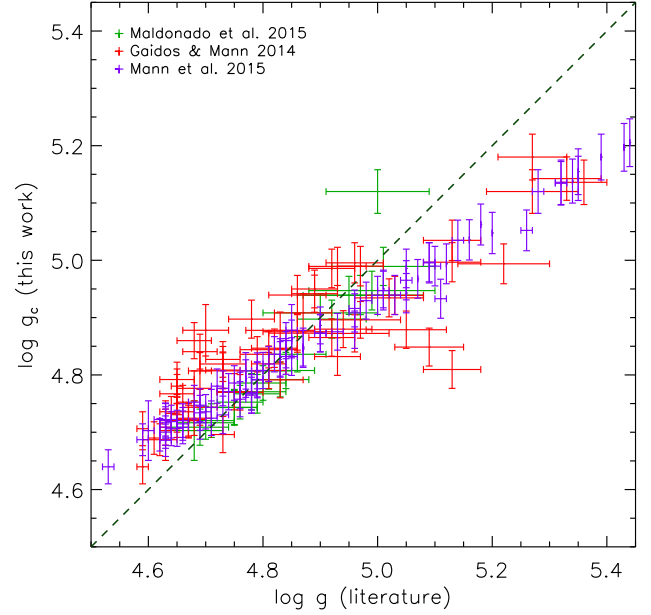

Fig. 7. Value of $\log g_c$ calculated using $\mathcal{M}_{M-R}$ from Sect. 3.4 and using R from Sect. 3.3 against $\log g$ from the literature.

by Mann et al. (2015) show a linear correlation to ours, although its slope is smaller than unity. Only the $\log g$ values derived from radii and masses published by Gaidos & Mann (2014) show a very weak correlation to ours. Since the $\log g$ values that have recently been published by Rajpurohit et al. (2018) do not correlate with Pass18 or other literature values, we did not include these values in Fig. 7. When we now use $\log g_c$ as an input for our spectral analysis described in Sect. 3.2 and keep it fixed, the resulting effective temperatures (and metallicities) do not change significantly and, therefore, neither do the radii nor the masses determined in Sect. 3.

Despite the large error bars inherent in calculating $\mathcal{M}_{\log g}$, and the problems described above, this method should not be generally dismissed. With precise input data as we have here, the error bars of $\mathcal{M}_{\log g}$ become small enough so that the correlation in Fig. 5 becomes visible. However, since the $\mathcal{M}_{M-R}$ masses have a much smaller error bar than the $\mathcal{M}_{\log g}$ masses we decided to keep using $\mathcal{M}_{M-R}$.

4.2. Photometric masses ($\mathcal{M}_{M-K_s}$)

For M dwarfs well established mass-magnitude relations exist for infrared filters determined by Delfosse et al. (2000), Benedict et al. (2016), and most recently by Mann et al. (2019). The latter provided two variants: the first is independent of metallicity and the second one accounts for metallicities $-0.4 <$ [Fe/H] $< +0.3$ when using their conservative validity range for metallicity. Both are valid for $4.5\,\text{mag} < M_{K_s} < 10.5\,\text{mag}$, where M_{K_s} is the absolute magnitude in the 2MASS K_s band. Since they also compared their results extensively to the well-established (Mann et al. 2015) $\mathcal{M}-M_K$ relations of Delfosse et al. (2000) and Benedict et al. (2016) and found good (but not perfect, see below) agreement, and since we determined metallicities (Sect. 3.2) within the recommended range, we employed the metallicity dependent variant of Mann et al. (2019) by using their recommended software[10]. However,

[10] https://github.com/awmann/M_-M_K-

the metallicity independent relation yields only marginally different numbers. We list the resulting masses, $\mathcal{M}_{M-K_s}$, in Table B.1.

A comparison between our $\mathcal{M}_{M-R}$ masses and the photometrically determined masses $\mathcal{M}_{M-K_s}$ is given in Fig. 8. Except for individual outliers (which is discussed in Sect. 5.2), the two mass values agree very well. When we, alternatively, compare our $\mathcal{M}_{M-R}$ values with the masses obtained from the two relations of Delfosse et al. (2000) and Benedict et al. (2016), we find disagreement of just beyond the size of our error bars for $\mathcal{M}_{M-R} \gtrsim 0.3\,\mathcal{M}_\odot$ but agreement otherwise. This is the same result described by Mann et al. (2019), who found discrepancies of about 10% between their values and the values obtained from the two previous relations above $0.3\,\mathcal{M}_\odot$. For the remainder of this paper we use $\mathcal{M}_{M-R}$ since differences between $\mathcal{M}_{M-R}$ and $\mathcal{M}_{M-K_s}$ are small.

As mentioned before, Trifonov et al. (2018) in their planet analysis and Reiners et al. (2018a) in their sample overview based their stellar masses on a mass-magnitude relation, but used a combination of the Delfosse et al. (2000) and Benedict et al. (2016) relations together with *Gaia* DR1 parallaxes. Therefore, our $\mathcal{M}_{M-K_s}$ masses differ accordingly.

4.3. PARSEC-based masses ($\mathcal{M}_P$)

Another method we used consists of a Bayesian approach applied to the PARSEC library of stellar evolution models to infer stellar parameters, as performed by del Burgo & Allende Prieto (2018). We applied this technique to 262 targets from Table B.1, assuming solar metallicity, and with data for the SDSS r band, the 2MASS J band, and *Gaia* DR2 parallaxes to convert the apparent magnitudes J into M_J. The input parameters to feed the method were then M_J, $r - J$, and [Fe/H] $= 0.0 \pm 0.2$ dex. The uncertainty in the iron-to-hydrogen ratio is reasonable since it reflects the range of [Fe/H] that we found in Sect. 3.2 (see also Fig. 5 of Pass18), and most of our targets belong to the thin disc (Cortés-Contreras 2016) for which this is a typical range.
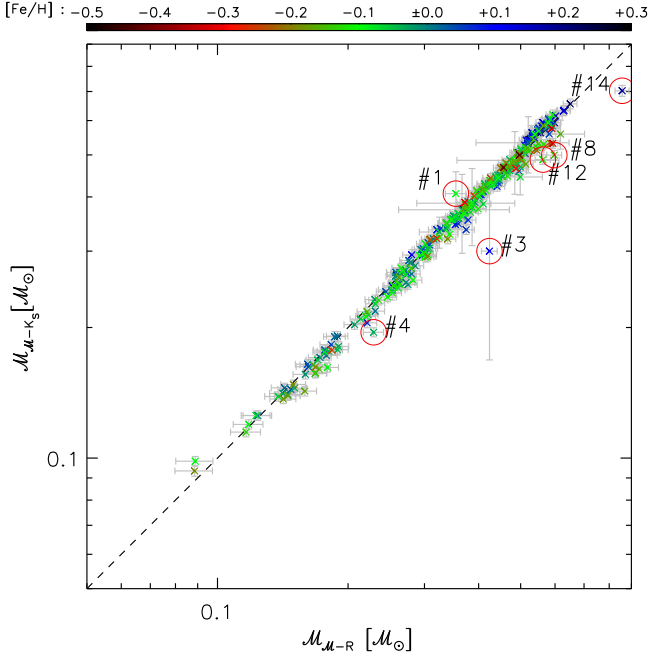
Fig. 8. Comparison of masses for all stars in Table B.1 using the method from Mann et al. (2019) as described in Sect. 4.2 on the *y*-axis and the method described in Sect. 3.4 on the *x*-axis. The metallicities are color coded as indicated. Obvious outliers, and stars discussed in reference to this figure in Sect. 5.2, are encircled: #1=Gl 411 (J11033+359), #3=GJ 4063 (J18346+401), #4=GJ 1235 (J19216+208), #8=1RXS J050156.7+010845 (J05019+011), #12=StKM 2-809 (J12156+526), and #14=K2-33 (J16102−193). See Fig. A.2 for a different comparison between the plotted values.

A grid of PARSEC isochrones (version 1.2S; Bressan et al. 2012; Chen et al. 2014, 2015; Tang et al. 2014) were downloaded and arranged, where [Fe/H] ranges from −2.18 to 0.47 in steps of 0.05 dex, age spans from 2 Myr to 13.1 Gyr with steps of 0.1%, and the initial mass runs from $0.09 \, \mathcal{M}_\odot$ to the highest mass established by the corresponding stellar lifetime.

This method yields mass, radius, luminosity, metallicity, age, and all derivable parameters. For this work we only use mass and radius and list these in Table B.1 as R_P and $\mathcal{M}_P$. The remaining results will be presented and discussed in a separate publication.

When we compare $\mathcal{M}_{\mathcal{M}-R}$ with $\mathcal{M}_P$ in Fig. 9 we find good correlation except for five outliers. They are the very young objects K2-33 (J16102−193), 1RXS J050156.7+010845 (J05019+011,) and RX J0506.2+0439 (J05062+046), and the two stars RBS 365 (J02519+224) and Gl 15A (J00183+440). All of these targets are discussed in Sect. 5.2 below. However, all $\mathcal{M}_P$ values are systematically slightly higher than $\mathcal{M}_{\mathcal{M}-R}$. This means that the $\mathcal{M}_P$ values are also systematically offset to the $\mathcal{M}_{\mathcal{M}-K_s}$ values in the same way.

Once again, for the remainder of this paper we use $\mathcal{M}_{\mathcal{M}-R}$ since systematic differences between $\mathcal{M}_{\mathcal{M}-R}$ and $\mathcal{M}_P$ do not change the overall picture, as described in Sect. 5.1.

5. Discussion

5.1. Sample properties

Having established a way to measure the masses of our targets, we investigate further statistical properties of our sample. When we use our results and produce a Hertzsprung–Russell diagram (HRD) in Fig. 10, we find all targets on the main sequence except
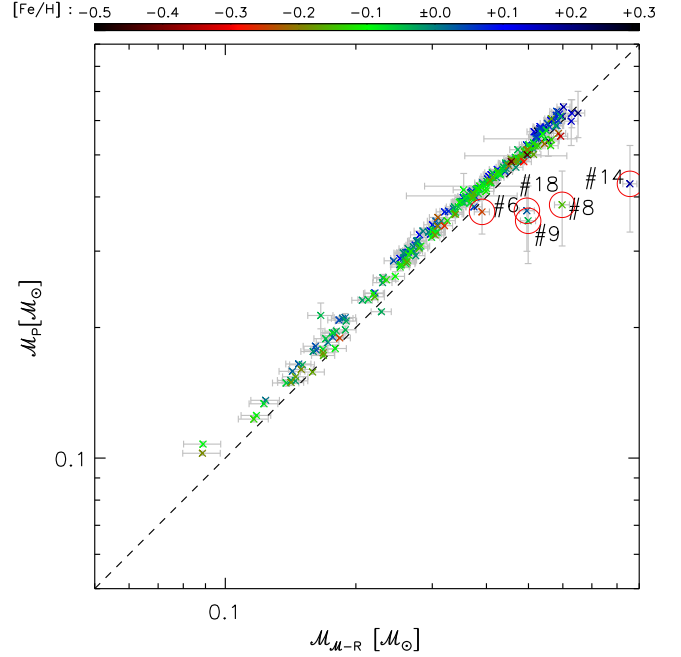
Fig. 9. Comparison of masses for all stars in Table B.1 using the method described in Sect. 4.3 on the *y*-axis and the method described in Sect. 3.4 on the *x*-axis. The metallicities are color coded as indicated. Obvious outliers, and stars discussed in reference to this figure in Sect. 5.2, are encircled: #6=Gl 15A (J00183+440), #8=1RXS J050156.7+010845 (J05019+011), #9=RX J0506.2+0439 (J05062+046), #14=K2-33 (J16102−193), and #18=RBS 365 (J02519+224).

for a few outliers. Most of these outliers are young. This is discussed on a case-by-case basis below.

Furthermore, when we plot $T_{\rm eff}$ against the mass of the star we find the relation shown in Figs. 11 and 12. While there is a large spread, the distribution is well consistent with the isochrones by BHAC15. Again, we can identify outliers, most of which are young or active, and all of these cases are discussed below. While the HRD only compares our independently determined luminosities L and effective temperatures $T_{\rm eff}$, Fig. 11 directly shows the results of our method described in Sect. 3.4.

Finally, when we plot the bolometric luminosity from Sect. 3.1 against the mass of the star to create a (bolometric) mass-luminosity relation we obtain Fig. 13. Again it is well consistent with the isochrones by BHAC15. When we fit a power law to these data for $0.1 \, \mathcal{M}_\odot < \mathcal{M}_{\mathcal{M}-R} < 0.5 \, \mathcal{M}_\odot$ we find a flat power law of

$$L \propto \mathcal{M}^{2.22\pm0.02}, \tag{10}$$

which deviates from power laws for L–$\mathcal{M}$ relations that average the whole main sequence yielding exponents of at least three. However, this agrees with results obtained for very low-mass stars that show a flattening of this power law at the bottom of the main sequence. This flattening can be seen already in, for example, Torres et al. (2010) or del Burgo & Allende Prieto (2018). As a recent example, Eker et al. (2018, and similarly the references therein) have derived a comparable exponent of 2.028 ± 0.135 for $0.179 \, \mathcal{M}_\odot < \mathcal{M} < 0.45 \, \mathcal{M}_\odot$. For $\mathcal{M}_{\mathcal{M}-R} \gtrsim 0.5 \, \mathcal{M}_\odot$ the relation in Fig. 13 clearly required a different exponent, but our high-mass range is too small to fit a reliable second power law.
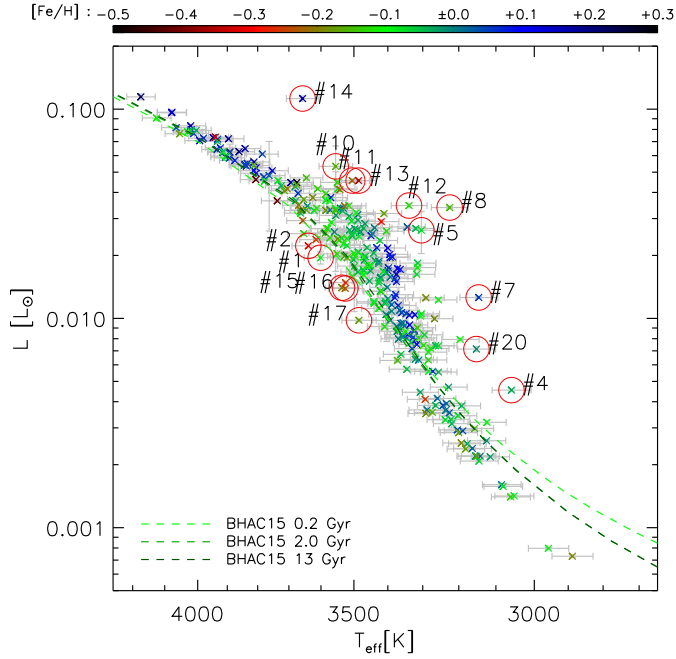
Fig. 10. Hertzsprung–Russell diagram using L from Sect. 3.1 and T_{eff} from Sect. 3.2. The metallicities are color coded as indicated. For comparison we plot isochrones for 0.2, 2, and 13 Gyr (in increasingly darker green) from BHAC15. Obvious outliers, and stars discussed in reference to this figure in Sect. 5.2, are encircled: #1=Gl 411 (J11033+359), #2=Gl 412A (J11054+435), #4=GJ 1235 (J19216+208), #5=2M J06572616+7405265 (J06574+740), #7=RX J0447.2+2038 (J04472+206), #8=1RXS J050156.7+010845 (J05019+011), #10=G 234-057 (J09133+688), #11=TYC 3529-1437-1 (J18174+483), #12=StKM 2-809 (J12156+526), #13=GJ 9520 (J15218+209), #14=K2-33 (J16102−193), #15=Gl 745A (J19070+208), #16=Gl 745B (J19072+208), #17=Gl 465 (J12248−182), and #20=LP 022-420 (J15499+796). Outliers #12 and #13 lie almost on top of each other. See Fig. A.3 for the same plot but using the pseudo equivalent width $pEW'_{H\alpha}$ of Schöfer et al. (2019) for the color coding. See also Fig. A.4 for a different comparison between the plotted values.

5.2. Outliers

Most of the outliers discussed in this section are young objects. They either belong to young associations or to young moving groups. Our $\mathcal{M}_{\mathcal{M}-R}$ values, however, are based on the assumption that the stars are older than a few hundred million years (cf. Sect. 3.4). The $\mathcal{M}_{\mathcal{M}-R}$ values that we list for these young objects should be treated accordingly. As Pass18 have already concluded, their effective temperatures are generally not affected by this assumption. Under the further assumption that the luminosity is not affected much either, the radii we list are not affected much by any assumptions regarding ages either. In other words, in cases in which we list or show a mass that is too high, we also derive a similarly large radius (cf. Eqs. 6 and 7), which may be expected for young objects.

Another set of the targets listed below are outliers and at the same time, some of their entries in at least one of the photometric catalogs are marked as being of bad quality. If such systematic errors were accounted for, our error bars would be increased significantly.

5.2.1. Data-based reasons

We first eliminate all outliers from our discussion that have data-based reasons for their designation as outliers because we do not wish to misidentify physical reasons.
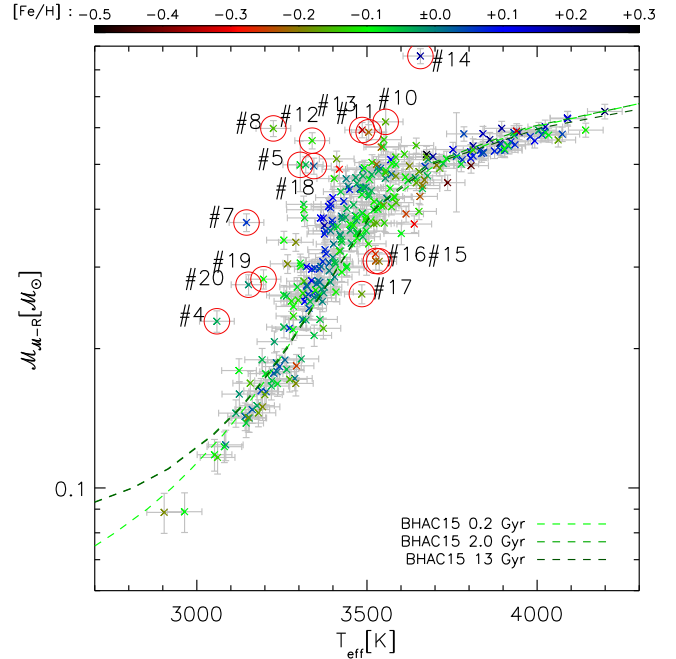

Fig. 11. Values of $\mathcal{M}_{\mathcal{M}-R}$ from Sect. 3.4 plotted against T_{eff} from Sect. 3.2. The metallicities are color coded as indicated. For comparison we plot isochrones for 0.2, 2, and 13 Gyr (in increasingly darker green) from BHAC15. Obvious outliers, and stars discussed in reference to this figure in Sect. 5.2, are encircled: #4=GJ 1235 (J19216+208), #5=2M J06572616+7405265 (J06574+740), #7=RX J0447.2+2038 (J04472+206), #8=1RXS J050156.7+010845 (J05019+011), #10=G 234-057 (J09133+688), #11=TYC 3529-1437-1 (J18174+483), #12=StKM 2-809 (J12156+526), #13=GJ 9520 (J15218+209), #14=K2-33 (J16102−193), #15=Gl 745A (J19070+208), #16=Gl 745B (J19072+208), #17=Gl 465 (J12248−182), #18=RBS 365 (J02519+224), #19=RX J1417.3+4525 (J14173+454), and #20=LP 022-420 (J15499+796). Outliers #12 and #13 lie almost on top of each other.
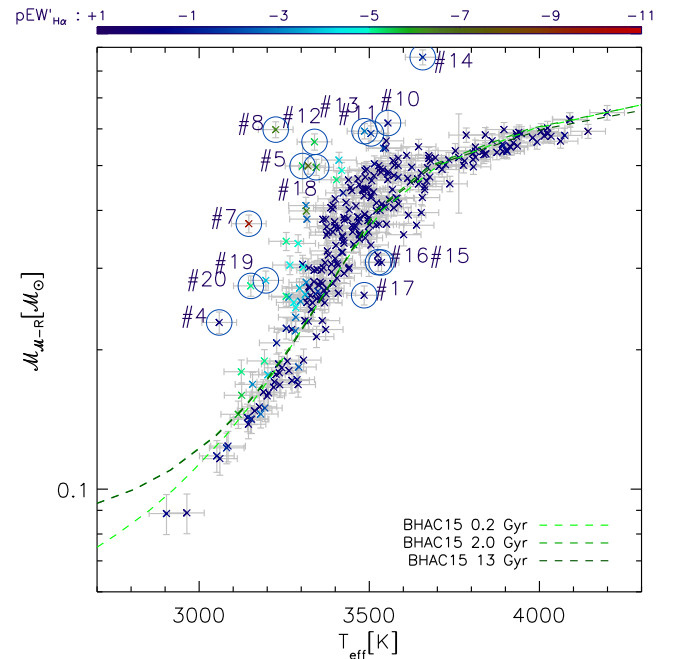

Fig. 12. Same as Fig. 11, but using the pseudo equivalent width $pEW'_{H\alpha}$ of Schöfer et al. (2019) for the color coding. Negative values of $pEW'_{H\alpha}$ denote Hα emission.
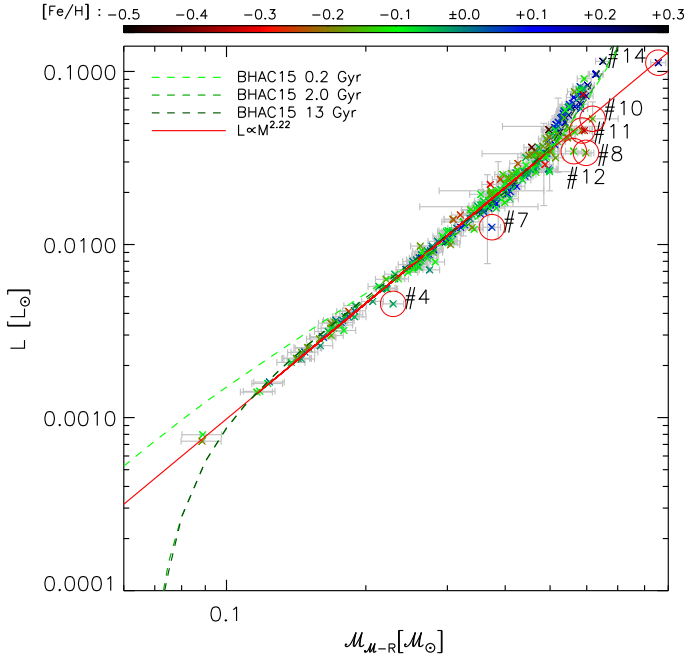
Fig. 13. Mass-luminosity relation using L from Sect. 3.1 and $\mathcal{M}_{\mathcal{M}-R}$ from Sect. 3.4. The metallicities are color coded as indicated. For comparison we plot isochrones for 0.2, 2, and 13 Gyr (dashed lines in increasingly darker green) from BHAC15. The red solid line indicates the fit we obtained in Eq. (10) Obvious outliers, and stars discussed in reference to this figure in Sect. 5.2, are encircled: #4=GJ 1235 (J19216+208), #7=RX J0447.2+2038 (J04472+206), #8=1RXS J050156.7+010845 (J05019+011), #10=G 234-057 (J09133+688), #11=TYC 3529-1437-1 (J18174+483), #12=StKM 2-809 (J12156+526), and #14=K2-33 (J16102−193).

#1=Gl 411 (J11033+359) and #2=Gl 412A (J11054+435). For these two stars we obtain different radii than measured interferometrically (cf. Sect. 3.3). Both are missing in the latest *Gaia* catalog, therefore we use parallaxes from the HIPPARCOS measurements. However, when comparing Eqs. (3) and (5) it is obvious that the distance does not cause a mismatch between the two different methods of computing radii. We confirm that by using the *Gaia* distance of Gl 412B for Gl 412A since both form a common proper motion pair. The values R and R_{interf} both changed slightly, but the data point in Fig. 3 only moved parallel to the 1–1-line, as expected.

Both stars have very reliable measurements of their effective temperatures since their fits described in Sect. 3.2 are of high quality. Furthermore, both T_{eff} agree well with the recent measurements of Mann et al. (2015) and Rajpurohit et al. (2018). Therefore, the reason for the mismatch to the very reliable interferometric radii must lie in the photometry. As a test, we took three stars from Table 1 that are in *Gaia* DR2 (Gl 15A, Gl 880 and Gl 699) and for which we obtain good results using *Gaia* parallaxes and photometry (cf. Sect. 3.3). But for this test we ignored all the *Gaia* bands B_P, G, and R_P, and calculated the luminosities with the remaining photometry. Using VOSA, we obtained different luminosities and, hence, radii that no longer agreed with their interferometric counterparts. This is because the *Gaia* filters anchor the SED very reliably in the optical while 2MASS and AllWISE anchor the SED in the infrared. In particular Gl 15A, which has unreliable 2MASS photometry (see below), showed the largest change in the test.

As a consequence of its uncertain luminosity, radius, and mass, Gl 411 also appears below the main sequence in the HRD

in Fig. 10 and is a mild outlier in Fig. 8. In addition to not having *Gaia* magnitudes, Gl 411 has also 2MASS and AllWISE magnitudes of poor quality because of its brightness. In both catalogs Gl 411 is listed to have magnitudes with low quality flags (DCD in 2MASS and UUAA in AllWISE). As described above, our error bars would have to be larger.

#3=GJ 4063 (J18346+401). This is an outlier when comparing $\mathcal{M}_{\mathcal{M}-R}$ to the absolute K_s band magnitude (cf. Fig. A.5). It is also one of the outliers when comparing $\mathcal{M}_{\mathcal{M}-R}$ with $\mathcal{M}_{\mathcal{M}-K_s}$ in Fig. 8. The reason for the deviations is the poor K_s-band photometry as indicated by the 2MASS quality flags (AAU).

#4=GJ 1235 (J19216+208). This object is an outlier in the HRD (Fig. 10), when plotting mass against effective temperature in Fig. 11 and in the $L - \mathcal{M}_{\mathcal{M}-R}$ plot in Fig. 13. However, we cannot explain this except by pointing out that this is a relatively faint, high proper motion star located in a crowded field where photometric contamination by background sources cannot be excluded.

#5=2MASS J06572616+7405265 (J06574+740). This object does not have a space-based parallax. We use the value obtained with the United States Naval Observatory Robotic Astrometric Telescope (Finch & Zacharias 2016), which is the only published trigonometric parallax and has a large relative error of 11%. Despite its large error bar, it is an outlier in the HRD (Fig. 10), and when plotting mass against effective temperature in Fig. 11. However, as an X-ray source (Haakonsen & Rutledge 2009) this is an active star (Ansdell et al. 2015; Schöfer et al. 2019), but we attribute its deviation in the diagrams instead to a wrong parallactic distance ($d = 26 \pm 3$ pc). In the literature, there have been at least four additional distance determinations from photometry and spectroscopy (Lépine & Gaidos 2011; Lépine et al. 2013; Cortés-Contreras 2016), and they all point toward a closer distance in the range $d = 14.0–19.6$ pc, which would lead to a luminosity and mass consistent with its measured effective temperature. We expect the next *Gaia* release to improve the precision of its luminosity and to help clarify its nature.

#6=Gl 15A (J00183+440). When plotting mass versus the J magnitude (Fig. A.6) this object is a mild outlier. However, it is also too bright in the infrared to have reliable 2MASS magnitudes as indicated by their quality flags (DCE).

5.2.2. Young age-based reasons

#7=RX J0447.2+2038 (J04472+206). This is one of the outliers in the HRD (Fig. 10) and when comparing mass against T_{eff} in Figs. 11 and 12. It is very active (Ishioka et al. 2014; Jeffers et al. 2018; Tal-Or et al. 2018), and Cortés-Contreras (2016) identified this object as a candidate member of the young disc population.

#8=1RXS J050156.7+010845 (J05019+011) and #9=RX J0506.2+0439 (J05062+046). The first is an outlier in all plots. It was identified by Schlieder et al. (2012a) to be a member of the β Pictoris moving group and, hence, very young. The second is a mild outlier and was identified by Schlieder et al. (2012b) as a candidate member of β Pictoris as well. These are two of the outliers in Fig. 9 comparing $\mathcal{M}_P$ to $\mathcal{M}_{\mathcal{M}-R}$. Their corresponding masses differ by about 30%. For the former the PARSEC-based method (cf. Sect. 4.3) yields for $\mathcal{M}_P = 0.38 \pm 0.08 \, \mathcal{M}_\odot$ an age of $\tau = 36 \pm 16$ Myr. For the latter the method yields for $\mathcal{M}_P = 0.35 \pm 0.07 \, \mathcal{M}_\odot$ an age of $\tau = 38 \pm 17$ Myr. Both ages are similar to the currently assumed age of β Pictoris of $\tau = 25 \pm 3$ Myr (e.g., Messina et al. 2016; Shkolnik et al. 2017).

#10=G 234-057 (J09133+688) and #11=TYC 3529-1437-1 (J18174+483). Both stars are noticeable outliers in almost all plots. However, both are young and candidate members of the AB Doradus association. The first was listed as a candidate by Schlieder et al. (2012b), and the second by Kastner et al. (2017). The second is also an active star discussed in Fuhrmeister et al. (2018).

#12=StKM 2-809 (J12156+526). This is an outlier in the $L - \mathcal{M}_{\mathcal{M}-R}$ plot in Fig. 13 and the HRD (Fig. 10). But again, this is an active (Stephenson 1986; Tal-Or et al. 2018), young star, which was identified as a candidate member of the Ursa Major moving group (Cortés-Contreras 2016).

#13=GJ 9520 (J15218+209). This is an outlier in almost every plot (e.g., in the HRD in Fig. 10), although not always an obvious one. It is an active (Fuhrmeister et al. 2018) and young star belonging to the Local Association (Tetzlaff et al. 2011).

#14=K2-33 (J16102−193). This is a pre-main-sequence star in the Upper Scorpius OB association. Its age is estimated to be between 5 and 20 Myr (David et al. 2016; Mann et al. 2016). It is a very obvious outlier in almost all plots. We measure unrealistic masses above $0.8 \, \mathcal{M}_\odot$ with all methods except that for obtaining $\mathcal{M}_P$ described in Sect. 4.3. Therefore, it appears as one of the outliers in Fig. 9. The PARSEC-based method yields $\mathcal{M}_P = 0.43 \pm 0.10 \, \mathcal{M}_\odot$ and at the same time an age of $\tau = 8.0 \pm 3.5$ Myr. Furthermore, it is by far the most distant target, and at a distance of $d \approx 140$ pc located in Upper Scorpius, extinction can no longer be neglected.

5.2.3. Examples of possible surprising results

While the stars discussed in this section are not obvious outliers, they demonstrate certain physical effects that can result in unexpected masses or radii. Furthermore, these stars are only examples and not a comprehensive list. In particular the plots involving $T_{\rm eff}$ (Figs. 10, 11 and 12) show a natural spread (as already described by Pass18), and the decision on which star is an outlier in these plots would require a non-trivial definition of a criterion.

#15=Gl 745A (J19070+208) and #16=Gl 745B (J19072+208). Both components of the wide binary system LDS 1017 are slightly below the main sequence in the HRD (Fig. 10). We also measure high effective temperatures for their derived masses when comparing these two parameters in Fig. 11. Together with very low activity they show a behavior akin to subdwarfs. Our derived [Fe/H] $= -0.20 \pm 0.16$ dex and [Fe/H] $= -0.23 \pm 0.16$ dex, respectively, also point toward low-metallicity objects. Furthermore, Mann et al. (2015) derived for Gl 745A an even lower metallicity of [Fe/H] $= -0.33 \pm 0.08$ dex, and Houdebine (2008) already classified both components as subdwarfs.

#17=Gl 465 (J12248−182). As the previous two stars, this isolated star is below the main sequence in the HRD and has a very high effective temperature for its derived mass (see Fig. 11). We measure [Fe/H] $= -0.17 \pm 0.16$ dex for this object. This metallicity is still too high to call it a subdwarf as it is still consistent with the solar. However, Maldonado et al. (2015) measured an even lower metallicity of [Fe/H] $= -0.33 \pm 0.09$ dex for this star.

#18=RBS 365 (J02519+224), #19=RX J1417.3+4525 (J14173+454) and #20=LP 022-420 (J15499+796). These three stars are mild outliers in the HRD (Fig. 10) or when plotting mass against $T_{\rm eff}$ (Figs. 11 and 12). These, however, are active stars that have, for instance, $\log L_{\rm H\alpha}/L_{\rm bol} > -4$ (Schöfer et al. 2019). The latter two are also in the CARMENES radial-velocity-loud sample discussed by Tal-Or et al. (2018).

5.3. How do the masses differ?

Overall, all methods in determining masses yield consistent results, even when using $\log g$ in order to obtain $\mathcal{M}_{\log g}$.

The largest amount of information is used in the construction of $\mathcal{M}_{\mathcal{M}-R}$ (Sect. 3.4) and in the construction of $\mathcal{M}_{\log g}$ (Sect. 4.1). The latter does not even use any empirical relation, however, it yields the largest error bars. Both $\mathcal{M}_{\mathcal{M}-R}$ and $\mathcal{M}_{\mathcal{M}-K_s}$ (Sect. 4.2) use an empirical relation. However, the $\mathcal{M}-R$ relation is more fundamental than the mass-magnitude relation. Mass and radius are fundamentally connected via the hydrostatics of a star, whereas a magnitude is an "arbitrary" portion of the SED. It is not fundamentally obvious that the luminosity within a restricted wavelength range uniquely relates to the mass of a star. Of course, these relations are well established and have been working very well (not to mention that they only require photometry and no spectroscopy). After all, the infrared magnitudes are representative of the luminosity of a star since similar relations between near-infrared magnitudes and luminosity are also well established, and an $\mathcal{M}-L$ relation is similarly fundamental as an $\mathcal{M}-R$ relation. In any case, our work can be considered an independent confirmation of the mass-magnitude relations of Mann et al. (2019), Benedict et al. (2016), or Delfosse et al. (2000).

It follows from the above discussion on the outliers that the age of a star also plays a significant role in testing the validity of any method intended for obtaining its mass and radius. All of these, except the PARSEC-based masses $\mathcal{M}_P$ (Sect. 4.3), assume an age of at least a few hundred megayears, i.e., that the stars have left the Hayashi track and reached the main sequence. Our spectral analysis (Sect. 3.2 and Pass18) assumes for the $\log g$ determination an age of 5 Gyr, which directly enters the spectroscopic mass $\mathcal{M}_{\log g}$. Both the mass-radius based masses $\mathcal{M}_{\mathcal{M}-R}$ and the photometric masses $\mathcal{M}_{\mathcal{M}-K_s}$ use empirical relations based on samples of old stars. This is in turn an advantage of the PARSEC-based masses $\mathcal{M}_P$ because, for example, the GTO targets of the β Pictoris moving group and the Upper Scorpius OB association have significantly lower $\mathcal{M}_P$ values than all the other masses. At the same time the method for obtaining $\mathcal{M}_P$ yields young ages for these sources. However, a detailed investigation of the validity and consequences of the combined determination of all parameters of M dwarfs (and the CARMENES targets in particular) using this method is beyond the scope of this paper and will be discussed in a separate publication. Therefore, we do not list the ages determined with this method except for the few examples above. On the other hand, old stars such as the potential subdwarfs mentioned above do not pose a problem for our method. In particular, as described in Sect. 3.4, our mass-radius relation does not differ for different ages above a few hundred million years, nor can we infer a metallicity dependence down to metallicities of globular clusters.

Besides the age constraints inherent in the different methods, there are further biases that enter some of the methods as already indicated in the introduction. Both $\mathcal{M}_{\mathcal{M}-R}$ and $\mathcal{M}_{\mathcal{M}-K_s}$ use empirical relations based on binaries. However, the mass-radius relation for $\mathcal{M}_{\mathcal{M}-R}$ uses close binaries, while the mass-luminosity relation for $\mathcal{M}_{\mathcal{M}-K_s}$ is measured using wide binaries. The latter is certainly a better representation for isolated
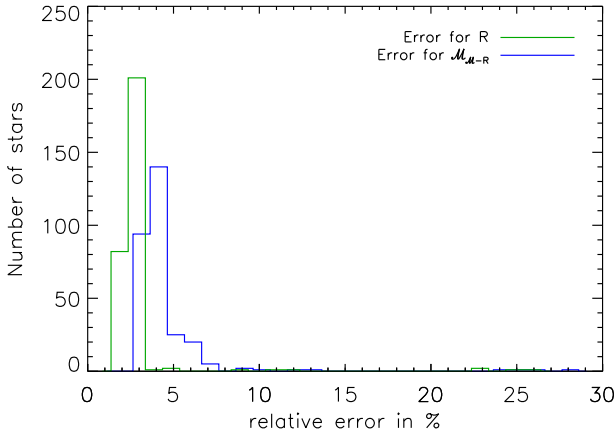
Fig. 14. Histograms of the errors of R and $\mathcal{M}_{M-R}$.

M dwarfs, i.e., our targets. If the former suffers from, for example, inflated radii then there is a systematic difference between $\mathcal{M}_{M-R}$ and $\mathcal{M}_{M-K_s}$. Such inflated radii have been reported (e.g., Jackson et al. 2018; Kesseli et al. 2018, and for eclipsing binaries by Parsons et al. 2018), but only for young, magnetically active, or fast-rotating stars. Our sample, however, mostly includes old, inactive, and slowly rotating stars (see Sect. 2). But if such a bias exists within the mass-radius relation derived in Sect. 3.4, it introduces an offset in our $\mathcal{M}_{M-R}$ values. As shown in Sect. 4.2 we find no offset between $\mathcal{M}_{M-R}$ and $\mathcal{M}_{M-K_s}$, indicating no systematic difference between the mass-radius relation and the mass-magnitude relation, or the samples on which they are based.

Finally, as described in Sect. 3.2, the choice of a specific set of synthetic spectra in our spectral analysis may introduce another systematic offset on the order of our $\Delta T_{\rm eff}/T_{\rm eff}$ errors, or larger. But again, the agreement of our $\mathcal{M}_{M-R}$ with the $\mathcal{M}_{M-K_s}$ that we observe indicates that we did not introduce such a systematic offset.

6. Conclusions

We have derived radii and masses with individual error bars for 293 of the CARMENES GTO M dwarfs. In particular, for measuring the masses, we used several methods and compared them. For typical field stars that are not young, we list consistent masses with all methods. For our main method we list radii R that typically have errors of 2–3%, and masses $\mathcal{M}_{M-R}$ that typically have errors of 3–5% (cf. Fig. 14). Systematic uncertainties on the order of the error bars, however, cannot be fully excluded.

For young stars, $\mathcal{M}_{M-R}$ and $\mathcal{M}_{M-K_s}$ are not suitable since the applicable empirical relations are derived for old stars (and cannot easily be adapted for young stars). Therefore, $\mathcal{M}_{M-R}$ and $\mathcal{M}_{M-K_s}$ for any young star in our sample (and not only for the outliers discussed in Sect. 5.2) should be used with care. The identification of all young stars, or determining their membership in young moving groups, should it exist, is beyond the purpose of this paper and will be published in the future. Similarly, an age determination of any star (not only those of our sample) is challenging. For example, Veyette & Muirhead (2018) derived ages for some of the CARMENES targets. On the other hand, $\mathcal{M}_P$ is not restricted to a single age, and ages along with $\mathcal{M}_P$ can be determined simultaneously as described in Sect. 4.3. Finally, when age estimates are available, our method of obtaining $\log g$ will be able to use isochrones for the appropriate age. Then our $\mathcal{M}_{\log g}$ is also an option, at least when we will be able to reduce

the error bars of $\log g$ to be smaller than the current 0.07 dex, and when systematic effects of theoretical isochrones can be reduced.

Our methods for measuring R and $\mathcal{M}_{M-R}$ work best for a field star of at least a few hundred million years when we can spectroscopically determine a reliable $T_{\rm eff}$, when the parallax of the object is based on *Gaia* DR2, and when L is well anchored by *Gaia* and near-infrared photometry. Then, we can determine for the target with the latest spectral type in our sample, the M7 V object Teegarden's star $R = 0.107 \pm 0.004\,R_\odot$ and $\mathcal{M}_{M-R} = 0.089 \pm 0.009\,\mathcal{M}_\odot$, while we determine for our M0.0 V targets average values $R = 0.566 \pm 0.016\,R_\odot$ and $\mathcal{M}_{M-R} = 0.574 \pm 0.021\,\mathcal{M}_\odot$.

References

Allard, F., Homeier, D., & Freytag, B. 2012, Philos. Trans. R. Soc. London Ser. A, 370, 2765
Alonso-Floriano, F. J., Morales, J. C., Caballero, J. A., et al. 2015, A&A, 577, A128
Andersen, J. 1991, A&ARv, 3, 91
Ansdell, M., Gaidos, E., Mann, A. W., et al. 2015, ApJ, 798, 41
Baraffe, I., Chabrier, G., Allard, F., & Hauschildt, P. H. 1998, A&A, 337, 403
Baraffe, I., Homeier, D., Allard, F., & Chabrier, G. 2015, A&A, 577, A42
Baroch, D., Morales, J. C., Ribas, I., et al. 2018, A&A, 619, A32
Bass, G., Orosz, J. A., Welsh, W. F., et al. 2012, ApJ, 761, 157
Bayo, A., Rodrigo, C., Barrado, Y., & Navascués, D. 2008, A&A, 492, 277
Becker, A. C., Agol, E., Silvestri, N. M., et al. 2008, MNRAS, 386, 416
Bender, C. F., Mahadevan, S., Deshpande, R., et al. 2012, ApJ, 751, L31
Benedict, G. F., Henry, T. J., Franz, O. G., et al. 2016, AJ, 152, 141
Berger, D. H., Gies, D. R., McAlister, H. A., et al. 2006, ApJ, 644, 475
Blake, C. H., Torres, G., Bloom, J. S., & Gaudi, B. S. 2008, ApJ, 684, 635
Bouchy, F., Pont, F., Melo, C., et al. 2005, A&A, 431, 1105
Boyajian, T. S., McAlister, H. A., van Belle, G., et al. 2012a, ApJ, 746, 101
Boyajian, T. S., von Braun, K., van Belle, G., et al. 2012b, ApJ, 757, 112
Bressan, A., Marigo, P., Girardi, L., et al. 2012, MNRAS, 427, 127
Caballero, J. A., Montes, D., Klutsch, A., et al. 2010, A&A, 520, A91
Caballero, J. A., Cortés-Contreras, M., & Alonso-Floriano, F. J. 2016, 19th Cambridge Workshop on Cool Stars, Stellar Systems, and the Sun (CS19), 148
Carter, J. A., Fabrycky, D. C., Ragozzine, D., et al. 2011, Science, 331, 562
Casal, E. 2014, Master's Thesis (Spain: Universidad de La Laguna)
Chen, Y., Girardi, L., Bressan, A., et al. 2014, MNRAS, 444, 2525
Chen, Y., Bressan, A., Girardi, L., et al. 2015, MNRAS, 452, 1068
Clausen, J. V., Bruntt, H., Claret, A., et al. 2009, A&A, 502, 253
Cortés-Contreras, M. 2016, PhD Thesis (Spain: Universidad Complutense de Madrid)

Cortés-Contreras, M., Béjar, V. J. S., Caballero, J. A., et al. 2017, A&A, 597, A47
Creevey, O. L., Benedict, G. F., Brown, T. M., et al. 2005, ApJ, 625, L127
Cutri, R. M. 2014, VizieR Online Data Catalog, II/328
David, T. J., Hillenbrand, L. A., Petigura, E. A., et al. 2016, Nature, 534, 658
del Burgo, C., & Allende Prieto, C. 2018, MNRAS, 479, 1953
Delfosse, X., Forveille, T., Ségransan, D., et al. 2000, A&A, 364, 217
Díez Alonso, E., Caballero, J. A., Montes, D., et al. 2019, A&A, 621, A126
Dittmann, J. A., Irwin, J. M., Charbonneau, D., et al. 2017, ApJ, 836, 124
Eker, Z., Bakış, V., Bilir, S., et al. 2018, MNRAS, 479, 5491
Feiden, G. A., & Chaboyer, B. 2012, ApJ, 757, 42
Finch, C. T., & Zacharias, N. 2016, AJ, 151, 160
Fuhrmeister, B., Czesla, S., Schmitt, J. H. M. M., et al. 2018, A&A, 615, A14
Gaia Collaboration (Brown, A. G. A., et al.) 2016, A&A, 595, A2
Gaia Collaboration (Brown, A. G. A., et al.) 2018, A&A, 616, A1
Gaidos, E., & Mann, A. W. 2014, ApJ, 791, 54
Haakonsen, C. B., & Rutledge, R. E. 2009, ApJS, 184, 138
Hartman, J. D., Bakos, G. Á., Noyes, R. W., et al. 2011, AJ, 141, 166
Hartman, J. D., Quinn, S. N., Bakos, G. Á., et al. 2018, AJ, 155, 114
Hauschildt, P. H., & Baron, E. 1999, J. Comput. Appl. Math., 109, 41
Hełminiak, K. G., & Konacki, M. 2011, A&A, 526, A29
Henden, A. A., Levine, S., Terrell, D., & Welch, D. L. 2015, Am. Astron. Soc. Meeting Abstracts, 225, 336.16
Henry, T. J., & Donald, W. J. 1993, AJ, 106, 773
Høg, E., Fabricius, C., Makarov, V. V., et al. 2000, A&A, 355, L27
Houdebine, E. R. 2008, MNRAS, 390, 1081
Husser, T.-O., Wende-von Berg, S., Dreizler, S., et al. 2013, A&A, 553, A6
Iglesias-Marzoa, R., López-Morales, M., Arévalo, M. J., Coughlin, J. L., & Lázaro, C. 2017, A&A, 600, A55
Irwin, J. M., Quinn, S. N., Berta, Z. K., et al. 2011, ApJ, 742, 123
Ishioka, R., Wang, S.-Y., Zhang, Z.-W., et al. 2014, AJ, 147, 70
Jackson, R. J., Deliyannis, C. P., & Jeffries, R. D. 2018, MNRAS, 476, 3245
Jeffers, S. V., Schöfer, P., Lamert, A., et al. 2018, A&A, 614, A76
Kaluzny, J., Thompson, I. B., Rozyczka, M., et al. 2013, AJ, 145, 43
Kaluzny, J., Thompson, I. B., & Dotter, A. 2014, Acta Astron., 64, 11
Kaluzny, J., Thompson, I. B., Dotter, A., et al. 2015, AJ, 150, 155
Kaminski, A., Trifonov, T., Caballero, J. A., et al. 2018, A&A, 618, A115
Kastner, J. H., Sacco, G., Rodriguez, D., et al. 2017, ApJ, 841, 73
Kesseli, A. Y., Muirhead, P. S., Mann, A. W., & Mace, G. 2018, AJ, 155, 225
Korda, D., Zasche, P., Wolf, M., et al. 2017, AJ, 154, 30
Kraus, A. L., Tucker, R. A., Thompson, M. I., Craine, E. R., & Hillenbrand, L. A. 2011, ApJ, 728, 48
Lépine, S., & Gaidos, E. 2011, AJ, 142, 138
Lépine, S., Hilton, E. J., Mann, A. W., et al. 2013, AJ, 145, 102
Ligi, R., Creevey, O., Mourard, D., et al. 2016, A&A, 586, A94
López-Morales, M., & Ribas, I. 2005, ApJ, 631, 1120
López-Morales, M., & Shaw, J. S. 2007, in The Seventh Pacific Rim Conference on Stellar Astrophysics, ed. Y. W. Kang, ASP Conf. Ser., 362, 26
Lopez-Morales, M., Orosz, J. A., & Shaw, J. S. 2006, ApJ [arXiv:astro-ph/0610225]
Luque, R., Nowak, G., Pallé, E., et al. 2018, A&A, 620, A171
Maldonado, J., Affer, L., Micela, G., et al. 2015, A&A, 577, A132
Mann, A. W., Feiden, G. A., Gaidos, E., Boyajian, T., & von Braun, K. 2015, ApJ, 804, 64
Mann, A. W., Newton, E. R., Rizzuto, A. C., et al. 2016, AJ, 152, 61
Mann, A. W., Dupuy, T., Kraus, A. L., et al. 2019, ApJ, 871, 63
Messina, S., Lanzafame, A. C., Feiden, G. A., et al. 2016, A&A, 596, A29
Morales, J. C., Ribas, I., Jordi, C., et al. 2009, ApJ, 691, 1400

Morrissey, P., Conrow, T., Barlow, T. A., et al. 2007, ApJS, 173, 682
Muiños, J. L., & Evans, D. W. 2014, Astron. Nachr., 335, 367
Nagel, E., Czesla, S., Schmitt, J. H. M. M., et al. 2019, A&A, 622, A153
Nefs, S. V., Birkby, J. L., Snellen, I. A. G., et al. 2013, MNRAS, 431, 3240
Ochsenbein, F., Bauer, P., & Marcout, J. 2000, A&AS, 143, 23
Parsons, S. G., Gänsicke, B. T., Marsh, T. R., et al. 2018, MNRAS, 481, 1083
Passegger, V. M., Wende-von Berg, S., & Reiners, A. 2016, A&A, 587, A19
Passegger, V. M., Reiners, A., Jeffers, S. V., et al. 2018, A&A, 615, A6
Pont, F., Bouchy, F., Melo, C., et al. 2005, A&A, 438, 1123
Press, W. H., Teukolsky, S. A., Vetterling, W. T., & Flannery, B. P. 2007, Numerical Recipes 3rd Edition: The Art of Scientific Computing, 3rd edn. (New York, NY, USA: Cambridge University Press)
Quirrenbach, A. 2001, in The Formation of Binary Stars, eds. H. Zinnecker, & R. Mathieu, IAU Symp., 200, 539
Quirrenbach, A., Amado, P. J., & Caballero, J. A. 2014, Proc. SPIE, 9147
Quirrenbach, A., Amado, P. J., & Caballero, J. A. 2016, Proc. SPIE, 9908
Quirrenbach, A., Amado, P. J., & Ribas, I. 2018, Proc. SPIE, 10702
Rajpurohit, A. S., Allard, F., Rajpurohit, S., et al. 2018, A&A, 620, A180
Reiners, A., Zechmeister, M., Caballero, J. A., et al. 2018a, A&A, 612, A49
Reiners, A., Ribas, I., Zechmeister, M., et al. 2018b, A&A, 609, L5
Ribas, I. 2003, A&A, 398, 239
Ribas, I., Tuomi, M., Reiners, A., et al. 2018, Nature, 563, 365
Rodrigo, C., Solano, E., & Bayo, A. 2012, SVO Filter Profile Service Version 1.0, IVOA Working Draft 15 October 2012
Rojas-Ayala, B., Covey, K. R., Muirhead, P. S., & Lloyd, J. P. 2012, ApJ, 748, 93
Schlieder, J. E., Lépine, S., & Simon, M. 2012a, AJ, 144, 109
Schlieder, J. E., Lépine, S., & Simon, M. 2012b, AJ, 143, 80
Schöfer, P., Jeffers, S. V., Reiners, A., et al. 2019, A&A, 623, A44
Ségransan, D., Kervella, P., Forveille, T., & Queloz, D. 2003, A&A, 397, L5
Shkolnik, E. L., Allers, K. N., Kraus, A. L., Liu, M. C., & Flagg, L. 2017, AJ, 154, 69
Skrutskie, M. F., Cutri, R. M., Stiening, R., et al. 2006, AJ, 131, 1163
Stephenson, C. B. 1986, AJ, 92, 139
Tal-Or, L., Zechmeister, M., Reiners, A., et al. 2018, A&A, 614, A122
Tang, J., Bressan, A., Rosenfield, P., et al. 2014, MNRAS, 445, 4287
Taylor, M. B. 2005, in Astronomical Data Analysis Software and Systems XIV, eds. P. Shopbell, M. Britton, & R. Ebert, ASP Conf. Ser., 347, 29
Tetzlaff, N., Neuhäuser, R., & Hohle, M. M. 2011, MNRAS, 410, 190
Tognelli, E., Prada Moroni, P. G., & Degl'Innocenti, S. 2018, MNRAS, 476, 27
Tonry, J. L., Stubbs, C. W., Lykke, K. R., et al. 2012, ApJ, 750, 99
Torres, G. 2013, Astron. Nachr., 334, 4
Torres, G., & Ribas, I. 2002, ApJ, 567, 1140
Torres, G., Andersen, J., & Giménez, A. 2010, A&ARv, 18, 67
Torres, G., Sandberg Lacy, C. H., Pavlovski, K., et al. 2014, ApJ, 797, 31
Trifonov, T., Kürster, M., Zechmeister, M., et al. 2018, A&A, 609, A117
Vaccaro, T. R., Rudkin, M., Kawka, A., et al. 2007, ApJ, 661, 1112
van Altena, W. F., Lee, J. T., & Hoffleit, E. D. 1995, The General Catalogue of Trigonometric [stellar] Parallaxes (Yale University Observatory)
van Belle, G. T., Creech-Eakman, M. J., & Hart, A. 2009, MNRAS, 394, 1925
van Leeuwen, F. 2007, A&A, 474, 653
Veyette, M. J., & Muirhead, P. S. 2018, ApJ, 863, 166
von Braun, K., Boyajian, T. S., van Belle, G. T., et al. 2014, MNRAS, 438, 2413
Wenger, M., Ochsenbein, F., Egret, D., et al. 2000, A&AS, 143, 9
York, D. G., Adelman, J., Anderson, Jr., J. E., et al. 2000, AJ, 120, 1579
Zacharias, N., Finch, C. T., Girard, T. M., et al. 2013, AJ, 145, 44
Zechmeister, M., Reiners, A., Amado, P. J., et al. 2018, A&A, 609, A12
Zhou, G., Bayliss, D., Hartman, J. D., et al. 2015, MNRAS, 451, 2263
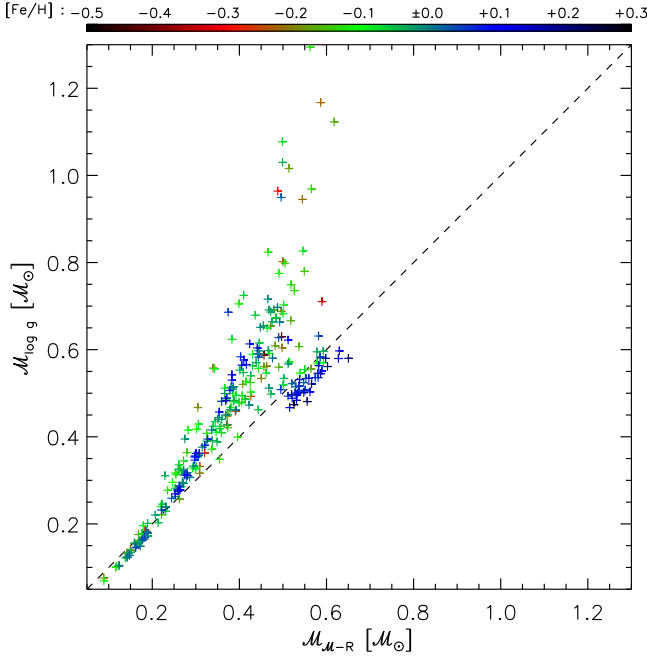
Appendix A: Additional figures

Fig. A.1. Same as Fig. 5, but without error bars for better clarity.

In this appendix, we provide supplemental material. First, we repeat Fig. 5 but we use linear axes and omit the error bars in Fig. A.1 for clarity.

Next, we resolve the confusion seen in Fig. 8 where all stars lie very close to the 1–1-line when plotting $\mathcal{M}_{M-K_s}$ against $\mathcal{M}_{M-R}$. Instead, in Fig. A.2 we now plot the ratio $\mathcal{M}_{M-K_s}$ over $\mathcal{M}_{M-R}$ against the metallicity from Sect. 3.2 and also take into account the activity of the stars using the pseudo equivalent width $pEW'_{H\alpha}$ of Schöfer et al. (2019) for the color coding. We can now identify that all $H\alpha$ emittiers have slightly higher $\mathcal{M}_{M-R}$ masses (and by Eqs. 6 and 7 also slightly larger radii) compared to the $\mathcal{M}_{M-K_s}$ masses. The $H\alpha$ absorbers, however, are symmetrically spread around a ratio of unity. There is a trend that the $\mathcal{M}_{M-R}$ masses are lower than the $\mathcal{M}_{M-K_s}$ masses only for the highest metallicities. A similar comparison of $\mathcal{M}_{M-R}$ with the other alternative masses $\mathcal{M}_{\log g}$ and $\mathcal{M}_P$, however, does neither show a trend with activity nor with metallicity in their deviation from $\mathcal{M}_{M-R}$.

We also repeat the HRD of Fig. 10 but using the pseudo equivalent width $pEW'_{H\alpha}$ of Schöfer et al. (2019) for the color coding in Fig. A.3. We again magnify the spread seen in the HRDs in Figs. 10 and A.3 by plotting the ratio L over $L_{BHAC15(13\,Gyr)}$ against the metallicity from Sect. 3.2 in Fig. A.4 and again taking into account the activity of the stars using the pseudo equivalent width $pEW'_{H\alpha}$ of Schöfer et al. (2019) for the color coding. This $L_{BHAC15(13\,Gyr)}$ is the luminosity of a star on the 13 Gyr isochrone from BHAC15 selected by its measured T_{eff}, i.e., the x-axis of the HRD in Fig. 10. Similar to Figs. 10 and A.3 we can identify that the active stars have the largest discrepancy from a theoretical, 13 Gyr old $L−T_{eff}$ sequence, and we can also see that all stars with [Fe/H] $\gtrsim 0.5$ dex are above the ratio of unity. The same behavior could be seen in a plot that magnifies the spread seen in Figs. 11 and 12 in an equivalent fashion but since no new information is revealed we omit such a plot.
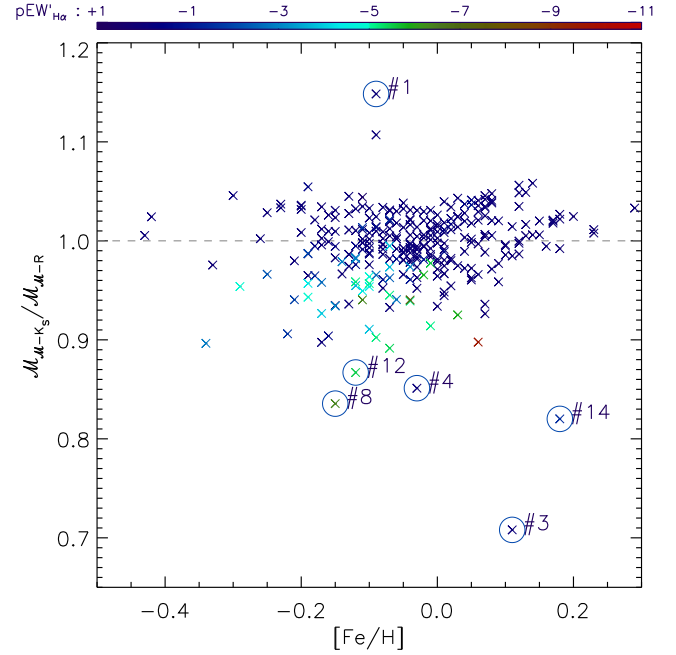

Fig. A.2. Ratio of the masses of Fig. 8 as a function of [Fe/H] using the pseudo equivalent width $pEW'_{H\alpha}$ of Schöfer et al. (2019) for the color coding. Negative values of $pEW'_{H\alpha}$ denote $H\alpha$ emission. Error bars are omitted for clarity. See Fig. 8 for the identification of the encircled stars.

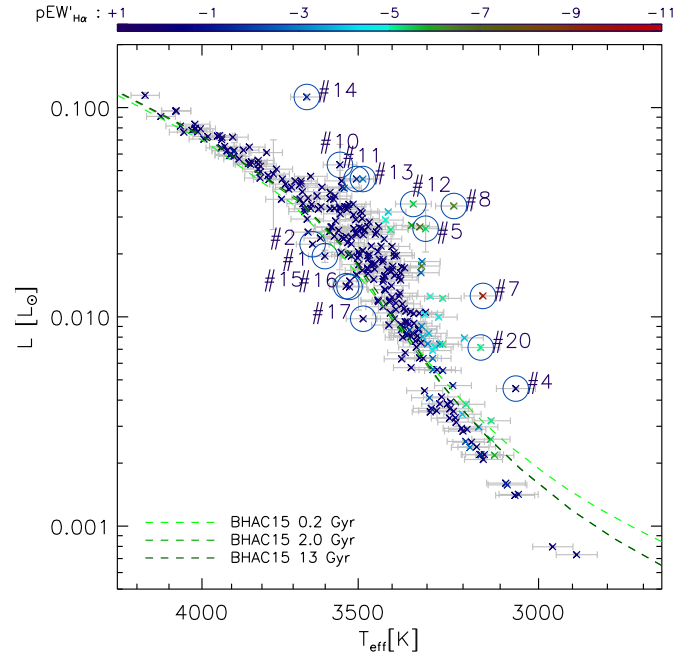**Fig. A.3.** Same as Fig. 10, but using the pseudo equivalent width $pEW'_{H\alpha}$ of Schöfer et al. (2019) for the color coding. Negative values of $pEW'_{H\alpha}$ denote $H\alpha$ emission. See Fig. 10 for the identification of the encircled stars.

We finally plot $\mathcal{M}_{M-R}$ against absolute magnitudes K_s and J in Figs. A.5 and A.6. These two plots help in identifying the outliers of Sect. 5.2.
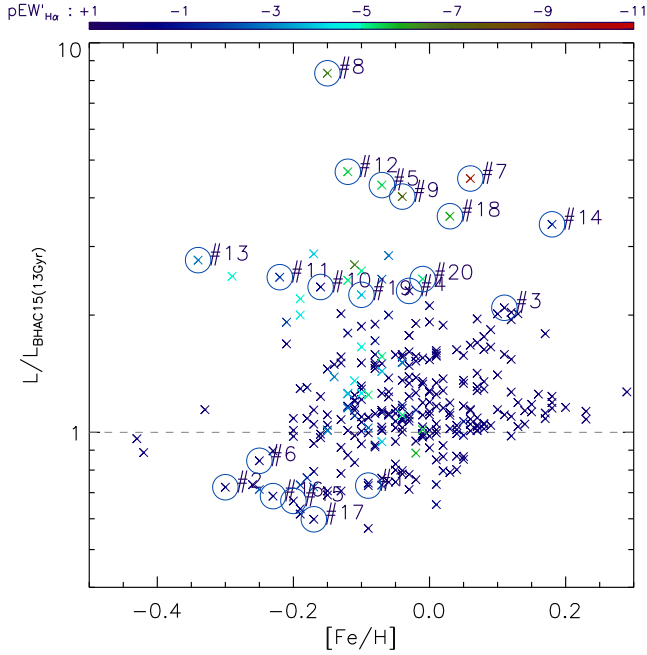
Fig. A.4. Ratio of the luminosity of the HRD in Fig. 10 and the luminosity of a 13 Gyr isochrone from BHAC15 for the measured effective temperatures as a function of [Fe/H] using the pseudo equivalent width $pEW'_{H\alpha}$ of Schöfer et al. (2019) for the color coding. Negative values of $pEW'_{H\alpha}$ denote Hα emission. Error bars are omitted for clarity. See Fig. 10 for the identification of the encircled stars.
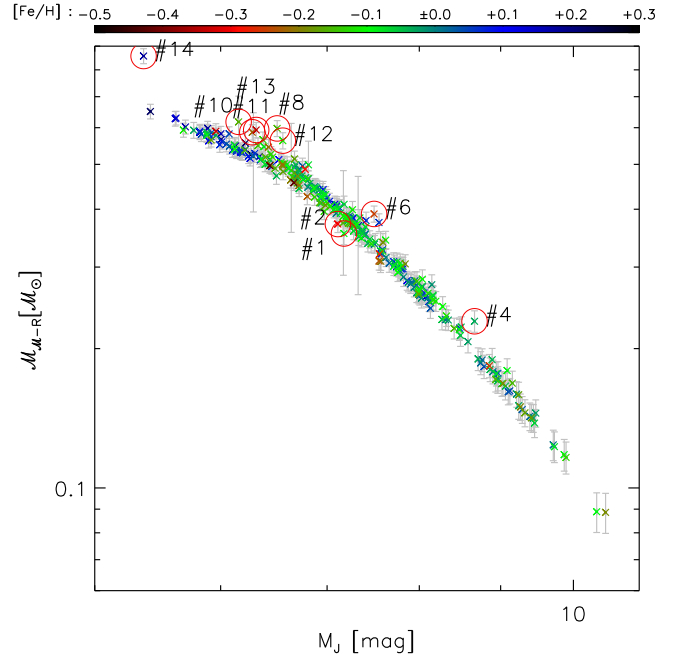

Fig. A.6. Value of $\mathcal{M}_{\mathcal{M}-R}$ against absolute J magnitude M_J. Obvious outliers, and stars discussed in reference to this figure in Sect. 5.2, are encircled: #1=Gl 411 (J11033+359), #2=Gl 412A (J11054+435), #4=GJ 1235 (J19216+208), #6=Gl 15A (J00183+440), #8=1RXS J050156.7+010845 (J05019+011), #10=G 234-057 (J09133+688), #11=TYC 3529-1437-1 (J18174+483), #12=StKM 2-809 (J12156+526), #13=GJ 9520 (J15218+209), and #14=K2-33 (J16102−193). Outliers #11 and #13 lie almost on top of each other.

Fig. A.5. Value of $\mathcal{M}_{\mathcal{M}-R}$ against absolute K_s magnitude M_{K_s}. Obvious outliers, and stars discussed in reference to this figure in Sect. 5.2, are encircled: #1=Gl 411 (J11033+359), #3=GJ 4063 (J18346+401), #4=GJ 1235 (J19216+208), #8=1RXS J050156.7+010845 (J05019+011), #10=G 234-057 (J09133+688), #11=TYC 3529-1437-1 (J18174+483), #12=StKM 2-809 (J12156+526), #13=GJ 9520 (J15218+209), and #14=K2-33 (J16102−193). Outliers #11 and #13 lie almost on top of each other.
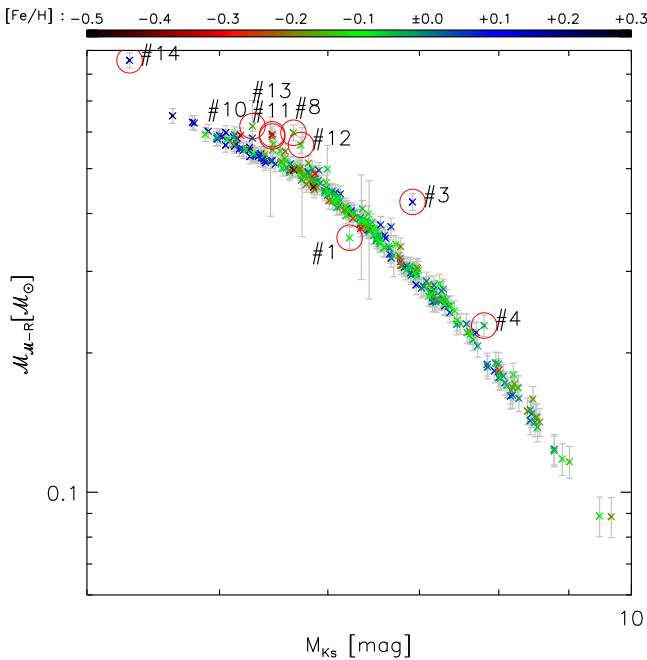
Appendix B: Additional table

Table B.2. Masses and radii of the eclipsing M dwarf binaries used to derive Eq. (6).

Name	RA (J2000)	Dec (J2000)	SpT [a]	$\mathcal{M}$ $(\mathcal{M}_\odot)$	R $(R_\odot)$	Ref.
OGLE-TR-122 B	11 06 51.89	−60 51 45.9	M	0.092 ± 0.009	0.120 ± 0.018	16
WTS 19g-4-02069 B	19 35 03.55	+36 31 16.5	M	0.143 ± 0.006	0.174 ± 0.006	20
LP 837-20 B	05 44 57.93	−24 56 09.7	M	0.179 ± 0.002	0.218 ± 0.011	19
LP 661-13 B	06 56 18.95	−08 35 46.5	M	0.19400 ± 0.00034	0.2174 ± 0.0023	18
Kepler-16 B	19 16 18.18	+51 45 26.8	M	0.1959 ± 0.0031	0.2262 ± 0.00056	4
OGLE-TR-125 B	10 57 51.86	−61 43 58.9	M	0.209 ± 0.033	0.211 ± 0.027	16
KOI-126 C	19 49 54.20	+41 06 51.4	M	0.2127 ± 0.0026	0.2318 ± 0.0013	7
CM Dra B	16 34 20.33	+57 09 44.4	M4.5	0.2141 ± 0.0010	0.2396 ± 0.0015	10
CM Dra A	16 34 20.33	+57 09 44.4	M4.5	0.2310 ± 0.0009	0.2534 ± 0.0019	10
SDSS-MEB-1 B	03 18 23.88	−01 00 18.4	M	0.240 ± 0.022	0.248 ± 0.009	5
KOI-126 B	19 49 54.20	+41 06 51.4	M	0.2413 ± 0.003	0.2543 ± 0.0014	7
LP 837-20 A	05 44 57.93	−24 56 09.7	M	0.244 ± 0.003	0.261 ± 0.009	19
1RXS J154727.5+450803 A	15 47 27.41	+45 07 51.3	M4	0.2576 ± 0.0085	0.2895 ± 0.0068	8
1RXS J154727.5+450803 B	15 47 27.41	+45 07 51.3	M4	0.2585 ± 0.0080	0.2895 ± 0.0068	8
OGLE-TR-5 B	17 51 49.34	−30 01 44.4	M	0.271 ± 0.035	0.263 ± 0.012	15
SDSS-MEB-1 A	03 18 23.88	−01 00 18.4	M	0.272 ± 0.020	0.268 ± 0.010	5
HAT-TR-318-007 B	08 50 32.96	+12 08 23.6	M5	0.2721 ± 0.0042	0.2913 ± 0.0024	24
LSPM J1112+7626 B	11 12 42.34	+76 26 56.4	M	0.2745 ± 0.0012	0.2978 ± 0.0050	1
OGLE-TR-7 B	17 52 08.66	−29 56 12.1	M	0.281 ± 0.029	0.282 ± 0.013	15
LP 661-13 A	06 56 18.95	−08 35 46.5	M3.5	0.30795 ± 0.00084	0.3226 ± 0.0033	18
LP 133-373 A	14 04 08.89	+50 20 38.7	M4	0.340 ± 0.014	0.33 ± 0.02	6
LP 133-373 B	14 04 08.89	+50 20 38.7	M4	0.340 ± 0.014	0.33 ± 0.02	6
OGLE-TR-6 B	17 51 03.07	−29 55 49.8	M	0.359 ± 0.025	0.393 ± 0.018	15
T-Cyg1-12664 B	19 51 39.82	+48 19 55.4	M	0.376 ± 0.017	0.3475 ± 0.0081	17
MOTESS-GNAT 2056316 B	23 14 38.16	+03 39 49.4	M3	0.382 ± 0.0023	0.374 ± 0.0035	2
OGLE-TR-18 B	17 54 16.46	−29 43 11.9	M	0.387 ± 0.049	0.390 ± 0.040	15
LSPM J1112+7626 A	11 12 42.34	+76 26 56.4	M4	0.3946 ± 0.0023	0.3860 ± 0.0050	1
CU Cnc B	08 31 37.57	+19 23 39.4	M3.5	0.399 ± 0.0015	0.391 ± 0.0104	12
CU Cnc A	08 31 37.57	+19 23 39.4	M3.5	0.433 ± 0.0017	0.432 ± 0.0052	12
MOTESS-GNAT 646680 B	10 30 55.21	+03 34 26.7	M2	0.443 ± 0.0020	0.427 ± 0.0061	2
HAT-TR-318-007 A	08 50 32.96	+12 08 23.6	M4	0.448 ± 0.001	0.4548 ± 0.0036	24
MOTESS-GNAT 2056316 A	23 14 38.16	+03 39 49.4	M2	0.469 ± 0.0023	0.441 ± 0.0035	2
Tres-Her0-07621 B	16 50 20.73	+46 39 01.4	M	0.489 ± 0.003	0.452 ± 0.06	13
MOTESS-GNAT 78457 B	03 26 20.73	+03 12 36.3	M4	0.491 ± 0.0018	0.471 ± 0.0111	2
Tres-Her0-07621 A	16 50 20.73	+46 39 01.4	M	0.493 ± 0.003	0.453 ± 0.06	13
NSVS 01031772 B	13 45 34.87	+79 23 48.3	M	0.498 ± 0.0022	0.509 ± 0.0026	25
MOTESS-GNAT 646680 A	10 30 55.21	+03 34 26.7	M1	0.499 ± 0.0020	0.457 ± 0.0070	2
MOTESS-GNAT 78457 A	03 26 20.73	+03 12 36.3	M3	0.527 ± 0.0018	0.505 ± 0.0111	2
WTS 19g-4-02069 A	19 35 03.55	+36 31 16.5	M3.5	0.530 ± 0.020	0.510 ± 0.010	20
MOTESS-GNAT 116309 B	04 48 09.63	+03 17 48.1	M0	0.531 ± 0.0016	0.532 ± 0.0073	2
MOTESS-GNAT 506664 B	07 43 11.57	+03 16 22.1	M2	0.544 ± 0.0016	0.513 ± 0.0068	2
MOTESS-GNAT 116309 A	04 48 09.63	+03 17 48.1	K8	0.567 ± 0.0015	0.552 ± 0.0102	2
MOTESS-GNAT 506664 A	07 43 11.57	+03 16 22.1	M1	0.584 ± 0.0015	0.560 ± 0.0039	2
V530 Ori B	06 04 33.8,	−03 11 52	M1	0.5955 ± 0.0022	0.5873 ± 0.0067	22
YY Gem A	07 34 37.58	+31 52 11.1	M1	0.597 ± 0.0034	0.619 ± 0.0040	11
GU Boo B	15 21 54.82	+33 56 09.1	M1	0.599 ± 0.0044	0.620 ± 0.014	9
YY Gem B	07 34 37.58	+31 52 11.1	M1	0.601 ± 0.0034	0.603 ± 0.0041	11
GU Boo A	15 21 54.82	+33 56 09.1	M1	0.609 ± 0.0050	0.623 ± 0.0112	9
2MASSJ01542930+0053266 B	01 54 29.30	+00 53 26.7	M1	0.62 ± 0.03	0.61 ± 0.09	14
Kepler-16 A	19 16 18.18	+51 45 26.8	K7	0.654 ± 0.017	0.6489 ± 0.0013	4
2MASSJ01542930+0053266 A	01 54 29.30	+00 53 26.7	M0	0.66 ± 0.03	0.64 ± 0.08	14
KIC 6131659 B	19 37 06.97	+41 26 12.8	M	0.685 ± 0.005	0.6395 ± 0.0061	21
ASAS J082552-1622.8 B	08 25 51.61	−16 22 47.4	M0	0.6872 ± 0.0049	0.699 ± 0.013	23
RXJ0239.1-1028 B	02 39 08.75	−10 27 46.4	K7	0.693 ± 0.006	0.703 ± 0.002	3
RXJ0239.1-1028 A	02 39 08.75	−10 27 46.4	K7	0.730 ± 0.009	0.741 ± 0.004	3

Notes. [a] The spectral types are the ones listed in SIMBAD or as given in the corresponding reference otherwise.

References. (1) Irwin et al. (2011); (2) Kraus et al. (2011); (3) López-Morales & Shaw (2007); (4) Bender et al. (2012); (5) Blake et al. (2008); (6) Vaccaro et al. (2007); (7) Carter et al. (2011); (8) Hartman et al. (2011); (9) López-Morales & Ribas (2005); (10) Morales et al. (2009); (11) Torres & Ribas (2002); (12) Ribas (2003); (13) Creevey et al. (2005); (14) Becker et al. (2008); (15) Bouchy et al. (2005); (16) Pont et al. (2005); (17) Iglesias-Marzoa et al. (2017); (18) Dittmann et al. (2017); (19) Zhou et al. (2015); (20) Nefs et al. (2013); (21) Bass et al. (2012); (22) Torres et al. (2014); (23) Hełminiak & Konacki (2011); (24) Hartman et al. (2018); (25) Lopez-Morales et al. (2006).